

Something something something physics

Steven Green
of Emmanuel College

A dissertation submitted to the University of Cambridge
for the degree of Doctor of Philosophy

Abstract

LHCb is a b-physics detector experiment which will take data at the 14 TeV LHC accelerator at CERN from 2007 onward...

Declaration

This dissertation is the result of my own work, except where explicit reference is made to the work of others, and has not been submitted for another qualification to this or any other university. This dissertation does not exceed the word limit for the respective Degree Committee.

Andy Buckley

Acknowledgements

Of the many people who deserve thanks, some are particularly prominent, such as my supervisor...

Preface

This thesis describes my research on various aspects of the LHCb particle physics program, centred around the LHCb detector and LHC accelerator at CERN in Geneva.

For this example, I'll just mention Chapter ?? and Chapter ??.

Contents

1. Calorimeter Optimisation Studies	1
1.1. Calorimeter Optimisation Studies	1
1.2. Metric	2
1.3. Simulation and Reconstruction	2
1.4. Calibration	2
1.5. Nominal Detector Performance	2
1.6. Electromagnetic Calorimeter Optimisation	3
1.6.1. ECal Transverse Granularity	4
1.6.2. ECal Longitudinal Granularity	6
1.6.3. ECal Active Material	9
1.7. Hadronic Calorimeter Optimisation	10
1.7.1. HCal Transverse Granularity	11
1.7.2. HCal Longitudinal Granularity	13
1.7.3. HCal Depth	15
2. The Sensitivity of CLIC to Anomalous Gauge Couplings through Vector Boson Scattering	19
2.1. Background	19
2.2. Generation	20
2.2.1. Cross Section Sensitivity	20
2.2.2. Event Weights	22
2.2.3. Validation of Samples	22
2.3. Simulation and Reconstruction	25
2.3.1. Experimental Conditions at CLIC	25
2.3.2. Beam-Related Backgrounds at CLIC	26
2.4. Analysis Processor and Jet Pairing	27
2.5. Methodology for Fitting	32
2.5.1. Choice of Fitting Distribution	32

2.5.2. Event Weight Impact on Fitting Distribution	33
2.5.3. Analysis of Fitting Distribution	34
2.6. Optimisation of Jet Reconstruction	36
2.6.1. 1.4 TeV Optimal Jet Reconstruction	36
2.6.2. 3 TeV Optimal Jet Reconstruction	37
2.7. Event Selection	39
2.7.1. Pre Selection - 1.4 TeV	41
2.7.2. MVA - 1.4 TeV	42
2.7.3. Pre Selection - 3 TeV	45
2.7.4. MVA - 3 TeV	45
2.8. Results	45
2.8.1. 1.4 TeV	45
A. Pointless extras	51
A.1. Anomalous Gauge Coupling Quartic Vertices Of Relevance in Vector Boson Scattering	51
A.2. χ^2 Contour Plots for Jet Algorithm Optimisation	54
Bibliography	63
List of figures	65
List of tables	69

*“Writing in English is the most ingenious torture
ever devised for sins committed in previous lives.”*

— James Joyce

Chapter 1.

Calorimeter Optimisation Studies

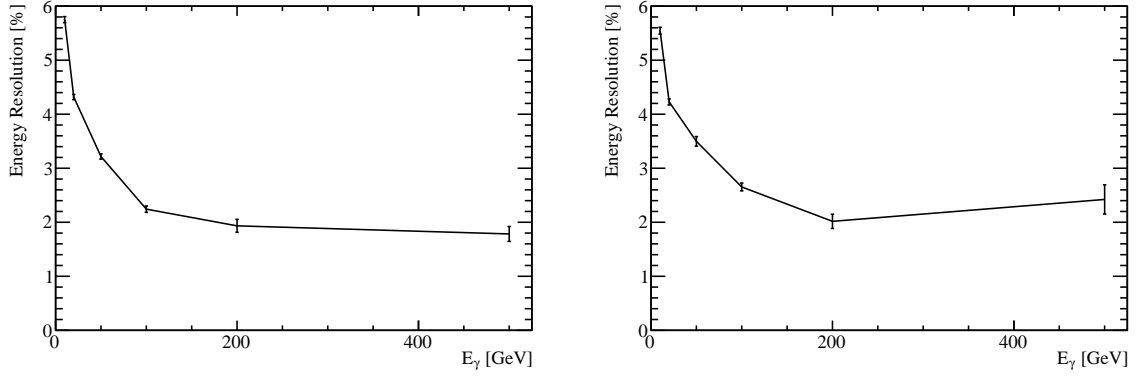
“There, sir! that is the perfection of vessels!”

— Jules Verne, 1828–1905

1.1. Calorimeter Optimisation Studies

If the future linear collider is to reach it’s maximum potential in terms of energy resolution then, optimisation of the detector will be essential. The energy resolution in the particle flow paradigm is dependant upon several detector components. The momentum of charged particles arises from the shape of the tracks deposited within the detector while the energy of uncharged particles arise from calorimetric measurements. Application of sophisticated pattern recognition algorithms allows the particle type to be inferred for the charged particles. In tern this allows for the conversion of the track momentum into an energy measure for the charged particles. The particle identification algorithms use the topological information acquired from the calorimetric energy deposited to infer particle type for a subset of charged particles.

The calorimetric energy deposits are therefore used in a twofold manner: (i) as energy measurements for neutral particles and (ii) as input for particle identification algorithms. There is potential for significant gains to be made in physics performance by optimising the calorimeters due to their dominant role in energy measurements. In this chapter the optimisation of the calorimeters is considered. Parameters such



(a) Silicon active material, $5 \times 5 \text{ mm}^2$ ECal transverse granularity. **(b)** Scintillator active material, $5 \times 5 \text{ mm}^2$ ECal transverse granularity.

Figure 1.1.: Energy resolution as a function of photon energy for the nominal ILD detector for both the silicon and scintillator options.

as the longitudinal granularity, transverse granularity and material choices for the calorimeters are considered.

This chapter concludes with an optimisation of several global parameters for the detector. These parameters are not calorimeter specific, but the optimisation procedure developed for the calorimeters is appropriate to use. These parameters relate to the global detector size and the magnetic field applied throughout solenoid in the detector.

1.2. Metric

1.3. Simulation and Reconstruction

1.4. Calibration

1.5. Nominal Detector Performance

The energy resolution for single photon events as a function of photon energy, for the nominal ILD detector, is shown in figure 1.1. The nominal jet energy resolution can be found in section BLAH.

1.6. Electromagnetic Calorimeter Optimisation

The ECal primarily measures the energy deposits of electromagnetic showers. The default ILD detector model ECal, summarised in table 1.1, contains 24 radiation lengths (X_0 , which acts to confine all but the highest energy electromagnetic showers within it. The longitudinal structure of this default model is 29 readout layers, consisting of pairs of active and absorber material, and one presampling layer, which exists to encourage shower development. Increasing the thickness of the absorber material part way into the detector reduces the number of readout channels and cost of the overall calorimeter while retaining a high sampling rate at the start of particle showers, which is crucial for the pattern recognition aspect of particle flow calorimetry.

Parameter	Default Value
Transverse Granularity	$5 \times 5 \text{ mm}^2$ square cells
Longitudinal Granularity	29 Readout Layers, 1 Presampling Layers
Active Material Choice	Silicon or Scintillator
Active Material Thickness	0.5 mm (Silicon) or 2 mm (Scintillator)
Absorber Material Choice	Tungsten
Absorber Material Thickness	20 Layers of 2.1 mm followed by 9 Layers of 4.2 mm

Table 1.1.: Nominal ILD detector model ECal configuration.

The parameters being optimised in this study are:

- Transverse granularity or cell size. This is a vital aspect of the detector in the particle flow paradigm as smaller cell sizes give greater potential for being able to separate energy deposits from charged and neutral particles. This transverse granularity should have little to no effect on the intrinsic energy resolution of the detector.
- Longitudinal granularity or cell depth. This parameter dictates the intrinsic energy resolution of the detector as smaller cell depths mean more sampling is done of the particle shower and so, due to the Poissonian statistics governing the measurement of particle showers, the better the resolution.
- Active material choice. This is a choice between silicon or scintillator. As well as providing different intrinsic energy resolutions the readout mechanics of these

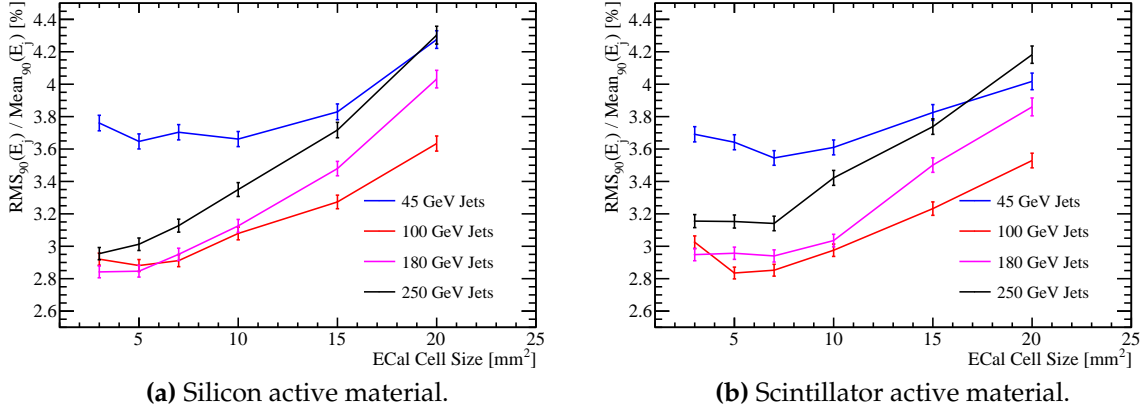


Figure 1.2.: Jet energy resolution as a function of ECal cell size for the silicon and scintillator ECal options.

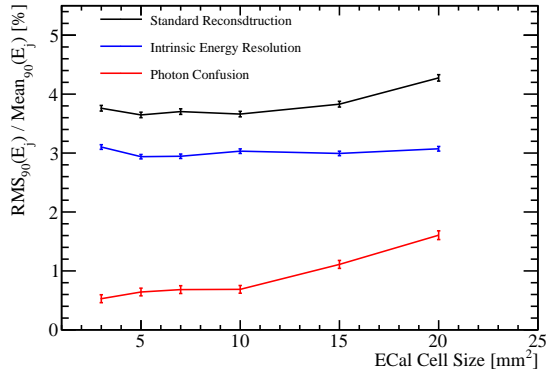
two options are significantly different. There is no clear prior knowledge as to which should provide better performance.

1.6.1. ECal Transverse Granularity

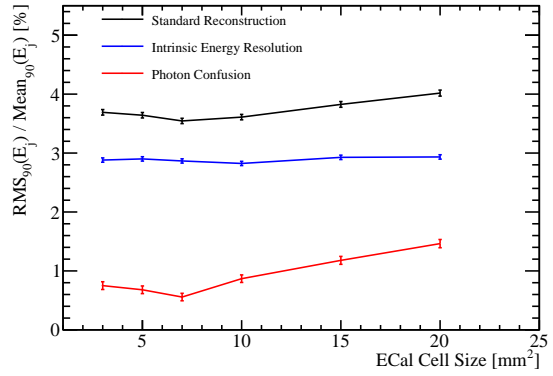
For this study a number of different detector models were considered where the transverse granularity in the ECal had been varied about the nominal value of $5 \times 5 \text{ mm}^2$ square cells. The granularities considered were $3 \times 3 \text{ mm}^2$, $5 \times 5 \text{ mm}^2$, $7 \times 7 \text{ mm}^2$, $10 \times 10 \text{ mm}^2$, $15 \times 15 \text{ mm}^2$ and $20 \times 20 \text{ mm}^2$ square cells for both the silicon and scintillator active material options. The jet energy resolution as a function of transverse granularity in the ECal is shown in figure 1.2.

The jet energy resolution was found to improve with decreasing cell size. This is expected as smaller cell size lead to better separation of energy deposits from neutral and charged particle showers.

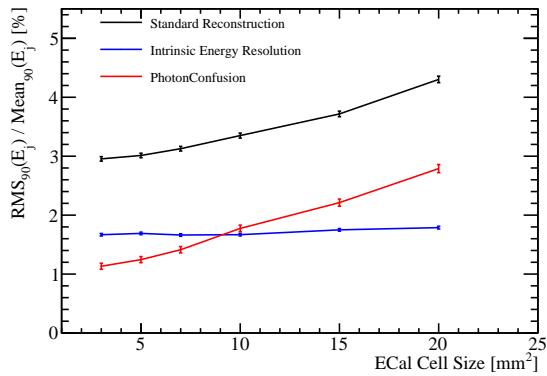
By examining the breakdown of the jet energy resolution into intrinsic resolution and confusion terms, as explained in chapter BLAH, it is possible to conclude that the dominant factor affecting the jet energy resolution when the transverse granularity of the ECal is varied is the confusion arising from photon energy deposits. Examples of jet energy resolution breakdowns are shown for 45 and 250 GeV jets for both the silicon and scintillator ECal options in figure 1.3. As expected in the intrinsic energy resolution does not change significantly with the transverse granularity.



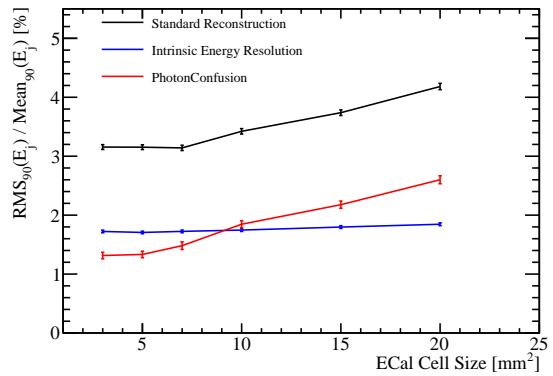
(a) Silicon active material, 45 GeV Jets.



(b) Scintillator active material, 45 GeV Jets.



(c) Silicon active material, 250 GeV Jets.



(d) Scintillator active material, 250 GeV Jets.

Figure 1.3.: Jet energy resolution breakdown as a function of ECal transverse granularity for 45 and 250 GeV jets. Results are given for both the silicon and scintillator ECal options.

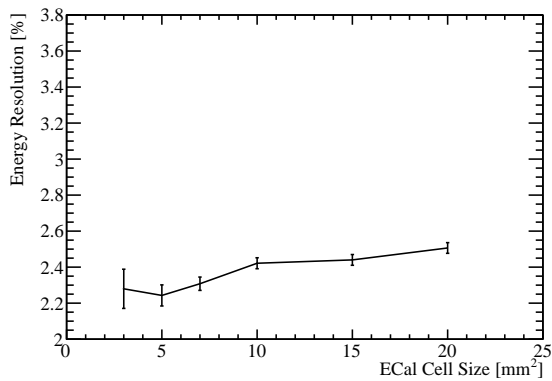
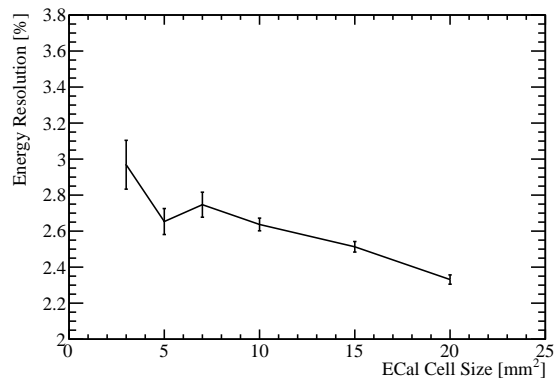
(a) Silicon active material, 100 GeV γ .(b) Scintillator active material, 100 GeV γ .

Figure 1.4.: Energy resolution as a function of ECal transverse granularity for 100 GeV photons. Results are given for both the silicon and scintillator ECal options.

A more targeted test of the intrinsic energy resolution of the ECal is presented in figure 1.4, which examines the energy resolution of single photon samples at 100 GeV. For the silicon option the intrinsic energy resolution was found to not vary significantly across the transverse granularities under consideration, however, there is a degradation in energy resolution with increasing cell size for the scintillator option. This originates from an inactive region of material in the simulation that represents the multi pixel photon counter (MPPC). The MPPC occupies a fixed area of the cell irrespective of cell size and so fractionally the "dead" region of the cell increases as cell size is reduced (cite this somehow). These trends will be present in the jet energy resolution studies, however, as only a small fraction, $\approx 10\%$, of the jet energy arises from the ECal these trends will be washed out when looking purely at jets.

In conclusion smaller transverse granularities in the ECal significantly improve the jet energy resolution for both the silicon and scintillator options. The intrinsic energy resolution of the ECal is largely invariant to changes in the transverse granularity for the silicon option, while larger transverse granularities are beneficial to the scintillator option as they reduce the impact of "dead" regions of the detector.

1.6.2. ECal Longitudinal Granularity

The performance of a number of detector configurations was examined where the longitudinal granularity of the ECal absorber material had been varied about the nominal value. This study was performed for both the silicon and scintillator active material options. In all cases considered tungsten was used as the absorber material in the ECal and the active layer thicknesses were not changed, that is 0.5 mm for the silicon option and 2 mm for the scintillator option. The layout of the ECal for detector models considered are summarised in table 1.2. For each detector model considered in this study the total number of radiation lengths in the ECal is kept approximately constant. This is done by varying the thickness of the absorber material when modifying the number of layers in the ECal.

The jet energy resolution was found to improve with increasing longitudinal granularity. This is expected as a more layers in the calorimeter, for the same total thickness, implies greater sampling of the particle shower and so, as the energy resolution obeys Poissonian statistics, an improvement in the intrinsic energy resolution is observed.

Total Number of Layers $N_{\text{Layers ECal}}$	N_{Layers} Region 1	Absorber Thickness Region 1 [mm]	N_{Layers} Region 2	Absorber Thickness Region 2 [mm]	Total Thickness [X_0]
30	20	2.10	9	4.20	22.77
26	17	2.40	8	4.80	22.60
20	13	3.15	6	6.30	22.47
16	10	4.00	5	8.00	22.31

Table 1.2.: Transverse granularity layout of various ECal models considered in this study. Radiation length of tungsten absorber is 3.504mm [12]. Note that the presampler layer contributes one layer to the cumulative number of layers value for all detector models considered.

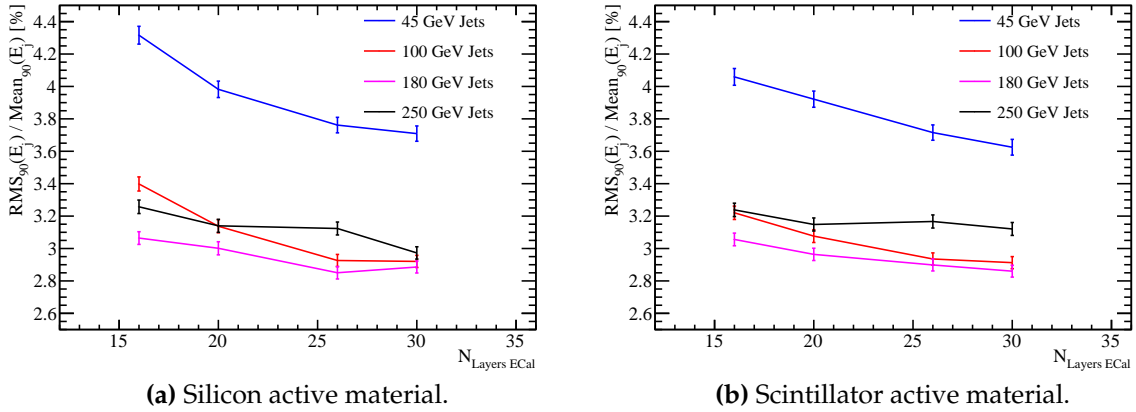
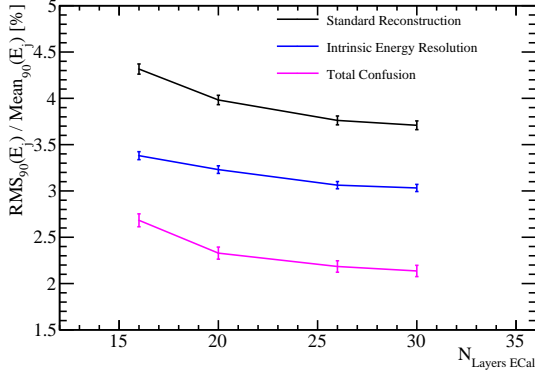


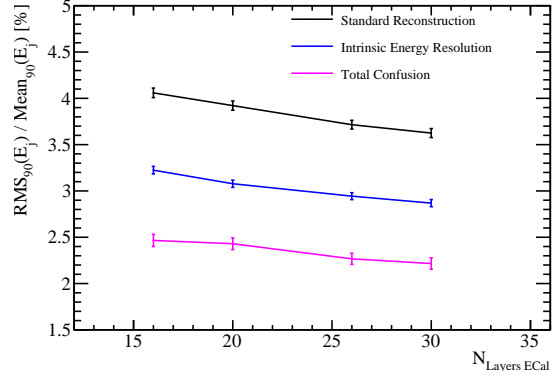
Figure 1.5.: Jet energy resolution as a function of longitudinal granularity in the ECal for the silicon and scintillator ECal options.

A particularly strong dependancy on ECal longitudinal granularity is noted at low energies, but this reduces significantly as energies rise.

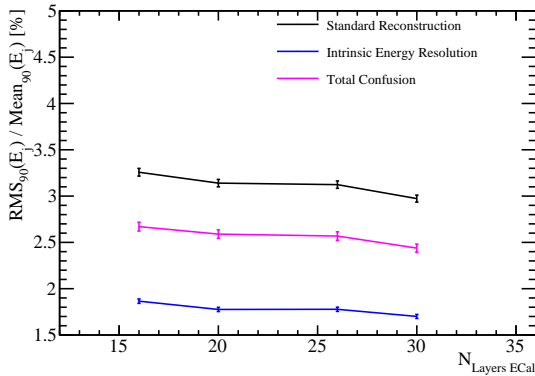
The strong dependancy of the jet energy resolution on the ECal longitudinal granularity can be expanded upon by looking at the decomposition of the jet energy resolution, which is shown in figure 1.6 for the 45 and 250 GeV energy jets. At low energies the trend is twofold: an improvement to the intrinsic energy resolution with more sampling of particle showers and a reduction in the impact of confusion. For high energy jets, where confusion dominates, there is little to no change in the intrinsic energy resolution and confusion as a function of ECal transverse granularity.



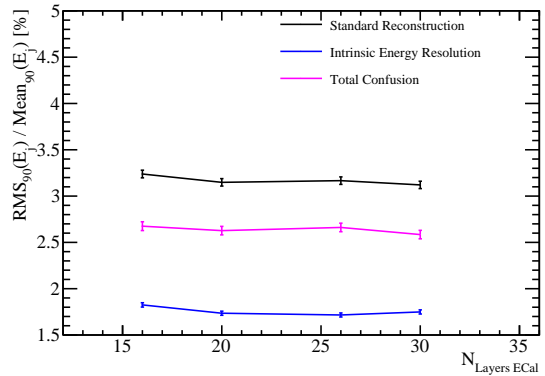
(a) Silicon active material, 45 GeV Jets.



(b) Scintillator active material, 45 GeV Jets.



(c) Silicon active material, 250 GeV Jets.



(d) Scintillator active material, 250 GeV Jets.

Figure 1.6.: Jet energy resolution breakdown as a function of ECal longitudinal granularity for 45 and 250 GeV jets. Results are given for both the silicon and scintillator ECal options.

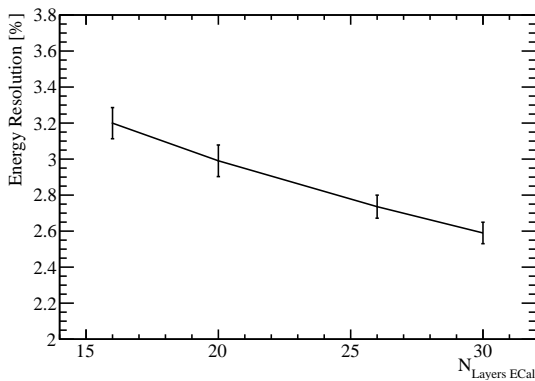
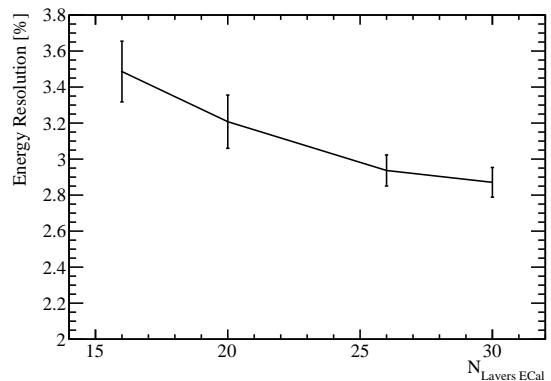
(a) Silicon active material, 100 GeV γ .(b) Scintillator active material, 100 GeV γ .

Figure 1.7.: Energy resolution as a function of function of ECal longitudinal granularity for 100 GeV photons. Results are given for both the silicon and scintillator ECal options.

Further understanding is gained by considering the energy resolution of single photon samples at 100 GeV as a function of the longitudinal granularity in the ECal, which is shown in figure 1.7. At these large photon energies it is clear that the intrinsic energy resolution of the ECal is improved by having finer longitudinal segmentation in the ECal. This trend will be present in the jet energy resolution study, but as only $\approx 10\%$ of the jet energy is measured in the ECal in comparison to $\approx 100\%$ of the photons energy, it will be obscured by the energy resolution of the rest of the detector, which is invariant to the ECal longitudinal segmentation.

The intrinsic energy resolution of the ECal is improved by having a finer transverse granularity. This is evident when looking at the energy resolution of photons whose energy deposits are localised within the ECal. This trend is again clear when considering the energy resolution of low energy jets, however, at higher energies the longitudinal granularity in the ECal is not a significant factor in determining detector performance.

1.6.3. ECal Active Material

In sections 1.6.1 and 1.6.2 the performance of the ECal was reported for both the silicon and scintillator options and to a large extent the performance of the two options was the same. There were a few differences, which attention should be brought to:

- The intrinsic energy resolution of a silicon ECal is worse than that of a scintillator ECal for low energies, while the trend is reversed at high energies. The cross over point in performance occurs between 20 and 50 GeV. This trend is shown in figure 1.1.
- The "dead" region due to the presence of the MPPC in the scintillator option degrades performance of the detector for small transverse granularities. No such effect is seen for the silicon option. This effect is shown in figure 1.4.

The lack of this "dead" region of the detector and the beneficial intrinsic energy resolution at large energies indicates a preference for a silicon detector, however, there is no clear preference based on these studies.

1.7. Hadronic Calorimeter Optimisation

The HCal is designed to measure the energy deposits from hadrons. The default ILD detector model HCal, summarised in table 1.3, contains ≈ 6 nuclear interaction lengths (λ_I). The ECal contributes approximately one λ_I giving a total of $\approx 7\lambda_I$, which is sufficient to confine the bulk of jets up to 1 TeV events, which is the maximum running energy for the ILC. The longitudinal structure of this model consists of 48 readout layers each containing a 3 mm active layer of scintillator and a 20 mm absorber layer of iron. There are several readout technology options under consideration for the HCal, which are analogue, digital and semi-digital, however, for this study only the analogue HCal is considered.

Parameter	Default Value
Transverse Granularity	$30 \times 30\text{mm}^2$ square cells
Longitudinal Granularity	48 Readout Layers
Active Material Choice	Scintillator Tiles
Active Material Thickness	3 mm
Absorber Material Choice	Steel
Absorber Material Thickness	20 mm

Table 1.3.: Nominal ILD detector model HCal configuration.

The parameters being optimised in this study are:

- Transverse granularity or cell size. This is key to successful application of pattern recognition in the particle flow paradigm, but should not change intrinsic energy resolution.
- Longitudinal granularity or cell depth. This governs the intrinsic energy resolution of a calorimeter.
- Depth of calorimeter. This is important in determining the impact of leakage of energy out of the detector.
- Sampling fraction. This is the ratio of the active medium thickness to the absorber medium thickness. As sampling calorimetry is based on sampling of particle showers it is expected that this is an important parameter. However, above a given sampling fraction there should be little difference between performance if

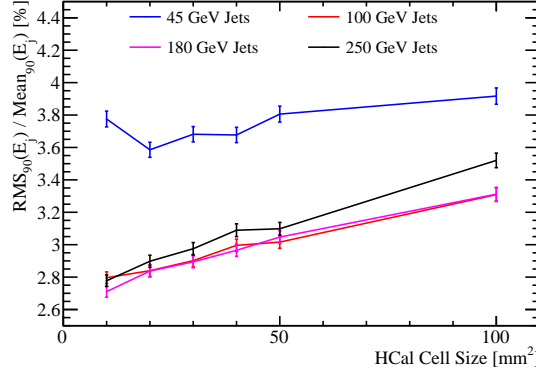


Figure 1.8.: Jet energy resolution as a function of HCal cell size.

showers are sampled at a high enough rate to get a good estimate of the incoming particles energy.

- **Absorber material choice.** This is a choice between steel or tungsten. While this does not change the active medium choice it does dictate the growth and propagation of showers and so plays a crucial role in calorimetry. While tungsten is more expensive than steel for the raw material the larger number of interaction lengths per length scale for tungsten mean that it is possible to create a smaller detector with the same number of interaction lengths within it. This reduces the size of the solenoid needed to generate the magnetic field and so lowers the price of the detector. As both of these materials are viable as absorber medium choices it is crucial to determine if either is more advantageous from a physics perspective.

1.7.1. HCal Transverse Granularity

For this study a number of different detector models were considered where the transverse granularity in the HCal had been varied about the nominal value of $30 \times 30 \text{ mm}^2$ square cells. The granularities considered were $10 \times 10 \text{ mm}^2$, $20 \times 20 \text{ mm}^2$, $30 \times 30 \text{ mm}^2$, $40 \times 40 \text{ mm}^2$, $50 \times 50 \text{ mm}^2$ and $100 \times 100 \text{ mm}^2$ square cells. The jet energy resolution as a function of transverse granularity in the HCal is shown in figure 1.8.

As with the case for the ECal, the jet energy resolution was found to improve with decreasing cell size as smaller cell size lead to better separation of energy deposits from neutral and charged particle showers.

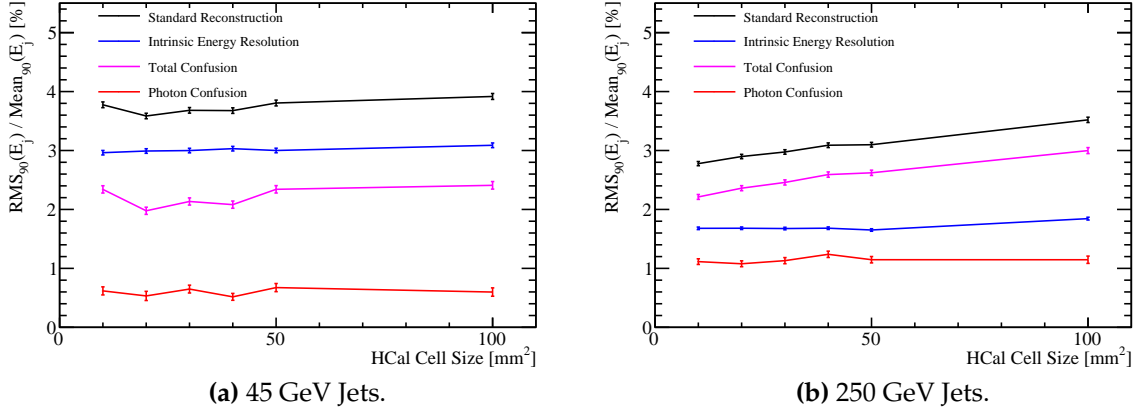


Figure 1.9.: Jet energy resolution breakdown as a function of HCal transverse granularity for 45 and 250 GeV jets.

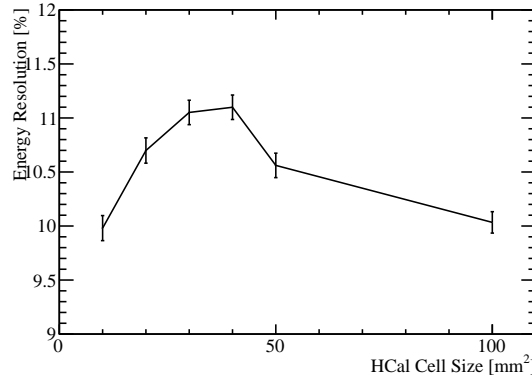


Figure 1.10.: Energy resolution as a function of HCal transverse granularity for 50 GeV K_L^0 .

The jet energy resolution breakdowns, shown in figure, 1.9, show that the confusion term varies when changing the HCal transverse granularity, but the intrinsic energy resolution does not. Furthermore, the photon confusion is invariant to changes in HCal transverse granularity, indicating that the observed overall performance changes are due to the effects of confusion arising from energy deposits from charged and neutral hadrons. Once again for 45 GeV jets the detector performance is dominated by intrinsic energy resolution and so HCal transverse granularity has little effect, while for 250 GeV jets the performance is dominated by confusion and HCal transverse granularity becomes more significant.

The energy resolution of single long lived neutral kaons, K_L^0 , at 50 GeV is considered as a function of transverse granularity in the HCal. This is shown in figure 1.10 and, as expected, the energy resolution of the detector is largely invariant to changes in

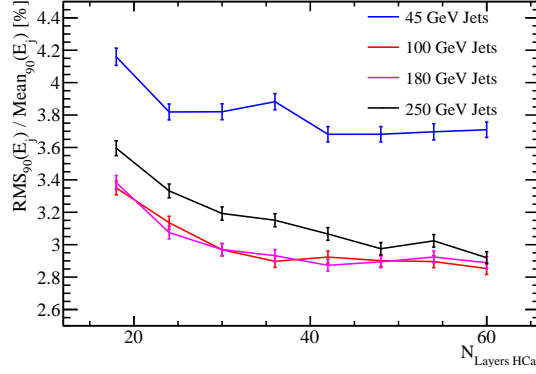


Figure 1.11.: Jet energy resolution as a function of longitudinal granularity in the HCal.

the transverse granularity in the HCal. As these K_L^0 samples may deposit energy in the ECal, this figure represents the intrinsic energy resolution of the ILD detector as a whole and not purely that of the HCal. However, it is expected that the bulk of the energy deposited by these samples occurs within the HCal and so such plots are a useful representation of the HCal performance.

The transverse granularity of the HCal acts to determine the impact of confusion from charged and neutral hadron energy deposits. It does not vary the intrinsic energy resolution of the detector, nor does it impact the reconstruction of photons. As confusion is dominant at high jet energies the HCal transverse granularity gains an increasing role in determining detector performance as the energy in an event increases.

1.7.2. HCal Longitudinal Granularity

A number of different detector models were examined where the longitudinal granularity of the HCal had been varied about the nominal value. In all cases the absorber material was steel while the active material was scintillator. Each HCal configuration had the same total number of nuclear interaction lengths, $5.72 \lambda_I$ in the absorber material and $0.19 \lambda_I$ in the active material, however, the thickness of the layers was varied depending on the total number of layers being considered. The ratio of the active material layers to the absorber material layers, the sampling fraction, was also kept constant in this study. A summary of the detector models considered in this study can be found in table 1.4.

Number $N_{\text{Layers HCal}}$	Absorber Thickness [mm]	Active Thickness [mm]
60	16.00	2.40
54	17.78	2.67
48	20.00	3.00
42	22.86	3.43
36	26.67	4.00
30	32.00	4.80
24	40.00	6.00
18	53.33	8.00

Table 1.4.: Transverse granularity layout of various HCal models considered.

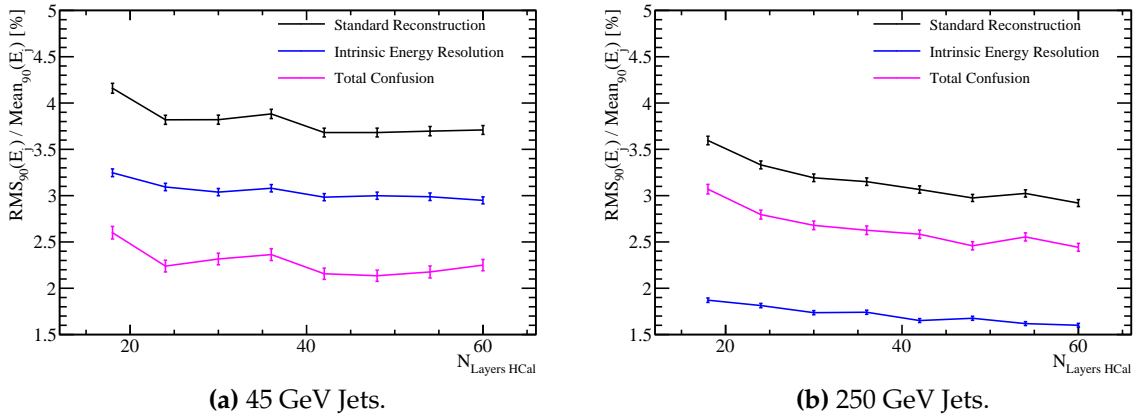


Figure 1.12.: Jet energy resolution breakdown as a function of HCal longitudinal granularity for 45 and 250 GeV jets.

The jet energy resolution for the various detector models considered is shown in figure 1.13. It was found that increasing the number of layers in the HCal, for the same total thickness, improved the jet energy resolution for all jet energies considered. Based on the increase in the frequency of sampling of particle showers in the HCal, it is expected that the intrinsic energy resolution of the detector should improve. However, the improvement observed in jet energy resolution for high energy jets indicates that longitudinal granularity is also affecting the confusion terms.

These trends are further explored by considering the breakdown of jet energy resolution, which are shown in figure 1.12. As expected from the standard performance reconstruction trends as a function of jet energy, there is an improvement in both the

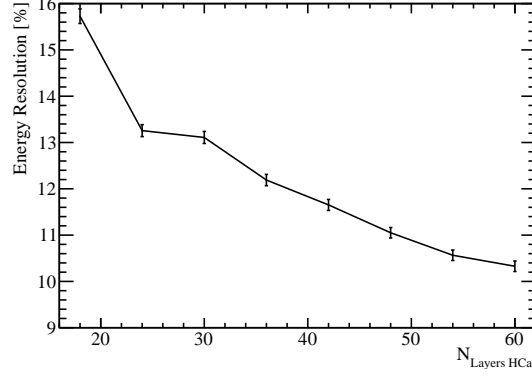


Figure 1.13.: Energy resolution as a function of HCal longitudinal granularity for 50 GeV K_L^0 .

intrinsic energy resolution and a reduction in the impact of confusion when the number of layers in the HCal is increased. The dominant trend driving the overall detector performance is that associated with the confusion of separating energy deposits from charged and neutral particles. This emphasises the importance of pattern recognition to detector performance in the particle flow paradigm.

The change in the intrinsic energy resolution of the HCal when varying the longitudinal granularity is best summarised by looking at the energy resolution of neutral hadrons as in the particle flow paradigm the energy of neutral hadrons is primarily measured in the HCal. A plot of energy resolution against the number of layers in the HCal for 50 GeV K_L^0 can be found in figure 1.13. This data shows that a reduction in sampling frequency of a particle shower that accompanies a reduction in the number of readout layers results in a broadening of energy distributions and a degradation in the resolution. It should again be emphasised that these results are for the full ILD detector model and so include the effect of the $\approx 1\lambda_I$ in the ECal.

The increasing the HCal longitudinal granularity has a twofold effect on the detector performance: an increase in sampling rate of particle showers and an improvement to the intrinsic energy resolution and a reduction in the confusion arising from associating energy deposits from hadrons.

1.7.3. HCal Depth

In this section the total depth of the HCal is varied about the nominal value of $5.72 \lambda_I$ keeping the total number of readout layers fixed at 48, the active material as scintillator,

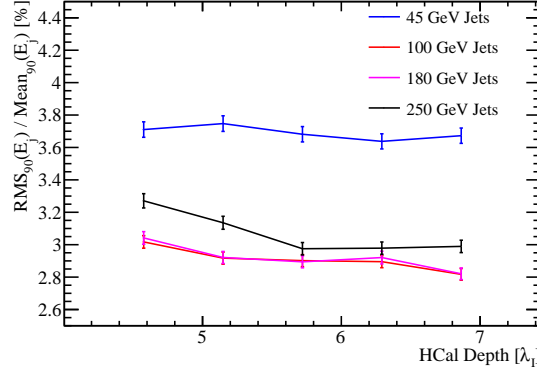


Figure 1.14.: Jet energy resolution is shown for several fixed energy jets as a function of the number of nuclear interaction lengths in the HCal.

the absorber material as iron and ratio of the thicknesses of the active to absorber layers fixed. The details of the detector models considered in this study can be found in table 1.5

HCal Depth [λ_I]	Absorber Thickness [mm]	Active Thickness [mm]
4.58	16	2.4
5.15	18	2.7
5.72	20	3.0
6.29	22	3.3
6.86	24	3.6

Table 1.5.: Depth and layout of various HCal models considered.

The jet energy resolution as a function of the total depth in the HCal is shown in figure 1.14. There is little variation in the detector performance as a function of the total depth of the HCal for all but the highest energy jets. At high jet energies there is a slight degradation in detector performance as the total thickness of the HCal is reduced.

Examining the breakdown of these trends at high energies, shown in figure 1.15, it becomes clear that the degradation in performance is due to confusion in associating energy deposits from hadrons. This is somewhat unexpected as it would be neutral to assume any improvements with a deeper HCal would be due to a reduction in the impact of leakage out of the back of the detector. This may be partially masked by

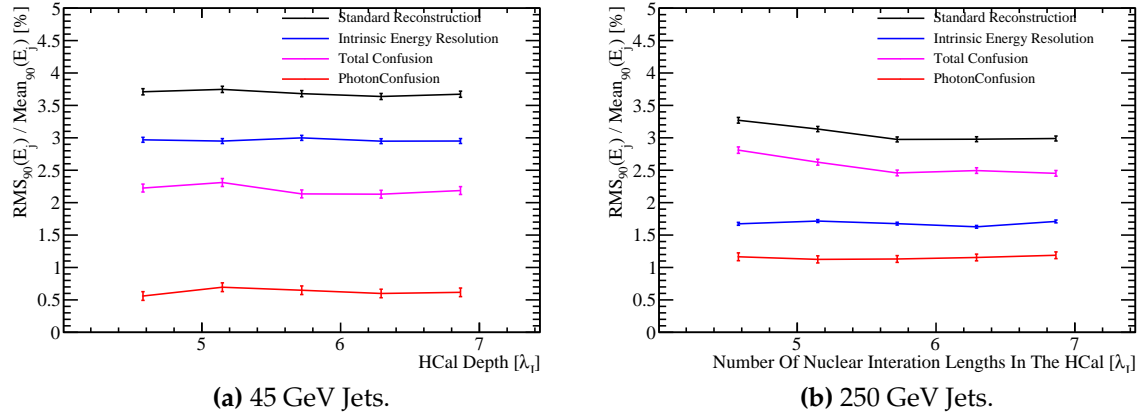


Figure 1.15.: Jet energy resolution breakdown as a function of nuclear interaction lengths in the HCal for 45 and 250 GeV jets.

the definition of RMS90 (PLOT?), however, it is clear that leakage is not a significant problem across the depth of HCals considered here for a typical event at these energies.

INTRINSIC ENERGY RESOLUTION FOR HIGH ENERGIES? HERE

Chapter 2.

The Sensitivity of CLIC to Anomalous Gauge Couplings through Vector Boson Scattering

“Kids, you tried your best, and you failed miserably. The lesson is, never try.”

— Homer Simpson

2.1. Background

A potential source of beyond the standard model physics that could be studied at the CLIC experiment is that of the anomalous gauge couplings α_4 and α_5 . The theoretical basis for these couplings is described in section THEORY REF. CLIC would show sensitivity to these couplings through vector boson scattering processes that are summarised in figures ??, ??, ?? and ??. An analysis of the sensitivity of CLIC to this processes is presented in the following chapter.

2.2. Generation

The event generation software used by the CLIC experiment is Whizard [7, 11]. Whizard version 1.97 was used for generating the new samples, while version 1.95 is used for the official CLIC samples. It was recommended by the Whizard authors to use version 1.97 as it contains a unitarisation scheme that ensures the probabilities remain physical up to high energies when considering the effect of anomalous gauge couplings.

The hadronic channels are the dominant decay modes of the W and the Z boson, with branching fractions of the order of 70% for both (REFERENCE PDG), and as the vector boson scattering is the desired signal channel, the focus of this analysis will be upon the hadronic decays of the W and Z. The vector boson scattering dominated signal final states containing hadronic decay products for the bosons are $\nu\nu qqqq$, $l\nu qqqq$ and $ll qqqq$.

2.2.1. Cross Section Sensitivity

To determine which final states are sensitive to α_4 and α_5 a comparison was made between the cross section using the standard model values of α_4 and α_5 , i.e. 0, and the same calculation using non-zero values of these couplings. This comparison was performed on all final states that would be relevant either as signal or background processes, for an analysis involving the purely hadronic decay channels of a vector boson scattering process. In full the states that were tested are:

- Vector boson scattering signal final states that are expected to show sensitivity to the anomalous couplings: $e^+e^- \rightarrow \nu\nu qqqq$, $e^+e^- \rightarrow l\nu qqqq$ and $e^+e^- \rightarrow ll qqqq$
- Four jet final states arising from e^+e^- interactions: $e^+e^- \rightarrow qqqq$.
- Two jet final states arising from e^+e^- interactions: $e^+e^- \rightarrow \nu\nu qq$, $e^+e^- \rightarrow l\nu qq$, $e^+e^- \rightarrow ll qq$ and $e^+e^- \rightarrow qq$.
- Four jet final states arising from the interactions of either e^+ or e^- with a beamstrahlung photon: $\gamma_{BS}e^- \rightarrow qqqqe^-$, $e^+\gamma_{BS} \rightarrow qqqqe^+$, $\gamma_{BS}e^- \rightarrow qqqq\nu$ and $e^+\gamma_{BS} \rightarrow qqqq\nu$.

- Four jet final states arising from the interactions of either e^+ or e^- with the electromagnetic field of the opposing beam particle. These cross sections are calculated using equivalent photon approximation (EPA), which represents the electromagnetic field of the opposing beam particle as a series of photon and so the final states appear as interactions of e^+ or e^- with photons: $\gamma_{\text{EPA}} e^- \rightarrow qqqqe^-$, $e^+ \gamma_{\text{EPA}} \rightarrow qqqqe^+$, $\gamma_{\text{EPA}} e^- \rightarrow qqqq\nu$ and $e^+ \gamma_{\text{EPA}} \rightarrow qqqq\nu$.
- Four jet final states arising from the interaction of the electromagnetic fields of opposing beam particles using the EPA approximation: $\gamma_{\text{EPA}} \gamma_{\text{EPA}} \rightarrow qqqq$.
- Four jet final states arising from the interaction of the electromagnetic field of either e^+ or e^- using the EPA approximation with a beamstrahlung photon: $\gamma_{\text{EPA}} \gamma_{\text{BS}} \rightarrow qqqq$ or $\gamma_{\text{BS}} \gamma_{\text{EPA}} \rightarrow qqqq$.
- Four jet final states arising from the interaction of two beamstrahlung photons: $\gamma_{\text{BS}} \gamma_{\text{BS}} \rightarrow qqqq$.

Note: In the above list $q = u, d, s, c$ and b , $l = e, \mu, \tau$ and $\nu = \nu_e, \nu_\mu$ and ν_τ .

The cross section was found to differ when using non-zero values for the anomalous couplings in comparison to the standard model prediction for the vector boson scattering signal final states $\nu\nu qqqq$, $l\nu qqqq$ and $ll qqqq$. The cross section comparisons for these final states can be found in table 2.1 and table 2.2 for 1.4 and 3 TeV samples respectively. In reality, non-zero anomalous couplings would change the cross sections of all processes considered, however, the sensitivity would only arise from high order terms in the Lagrangian. Such terms would not be dominant in determining the cross section and so are omitted from the generator making certain final states appear invariant to changes in the anomalous couplings.

The cross section calculations show that the most sensitive final state to the anomalous gauge couplings is $\nu\nu qqqq$, therefore, this analysis will focus solely upon this final state. Furthermore, as the $l\nu qqqq$ final state has a much reduced sensitivity in comparison to the $\nu\nu qqqq$ state and as the $ll qqqq$ can be easily vetoed from the analysis, as will be shown in subsequent chapters, it is only necessary to consider the sensitivity of the $\nu\nu qqqq$ final state. For the aforementioned reasons the $l\nu qqqq$ and $ll qqqq$ final states will be treated as backgrounds that are invariant to changes in the anomalous couplings α_4 and α_5 .

Final State	Cross Section [fb] ($\alpha_4 = \alpha_5 = 0.00$)	Cross Section [fb] ($\alpha_4 = \alpha_5 = 0.05$)	Percentage Change[%]	CLIC Cross Section [fb]
$e^+e^- \rightarrow \nu\nu qqqq$	20.8	34.6	+66.3	24.7
$e^+e^- \rightarrow l\nu qqqq$	112	113	+0.9	115.3
$e^+e^- \rightarrow ll qqqq$	59.7	68.6	+14.9	62.1

Table 2.1.: Cross section for selected processes for given value of α_4 and α_5 at 1.4 TeV.

Final State	Cross Section [fb] ($\alpha_4 = \alpha_5 = 0.000$)	Cross Section [fb] ($\alpha_4 = \alpha_5 = 0.005$)	Percentage Change[%]	CLIC Cross Section [fb]
$e^+e^- \rightarrow \nu\nu qqqq$	51.2	77.7	+51.8	71.5
$e^+e^- \rightarrow l\nu qqqq$	111.9	115.9	+3.6	106.6
$e^+e^- \rightarrow ll qqqq$	169.7	161.7	-4.9	169.3

Table 2.2.: Cross section for selected processes for given value of α_4 and α_5 at 3 TeV.

2.2.2. Event Weights

The sensitivity of an individual event to the anomalous gauge couplings is determined through an event weight. This weight is given by the ratio of the squares of the matrix element used in the cross section calculation, one matrix element using non-zero values of α_4 and α_5 and the other matrix element using the standard model values of α_4 and α_5 , i.e. 0. The weight varies as a function of α_4 and α_5 as well as varying on an event by event basis as the kinematics of the final state changes. Examples of the event weights as a function of α_4 and α_5 for selected events is shown in figure 2.4 for 1.4 TeV events.

This reweighting procedure has many advantages over the alternative of generating new samples with fixed α_4 and α_5 , notably the absence of systematic errors arising from new event generation, simulation and reconstruction.

2.2.3. Validation of Samples

The CLIC experiment has a repository of simulated and reconstructed samples that can be used for physics analyses, however, it is not possible to calculate the event weights for these samples as the raw Whizard format event files are missing. Therefore, a new $e^+e^- \rightarrow \nu\nu qqqq$ sample was generated with the relevant files to make reweighting as

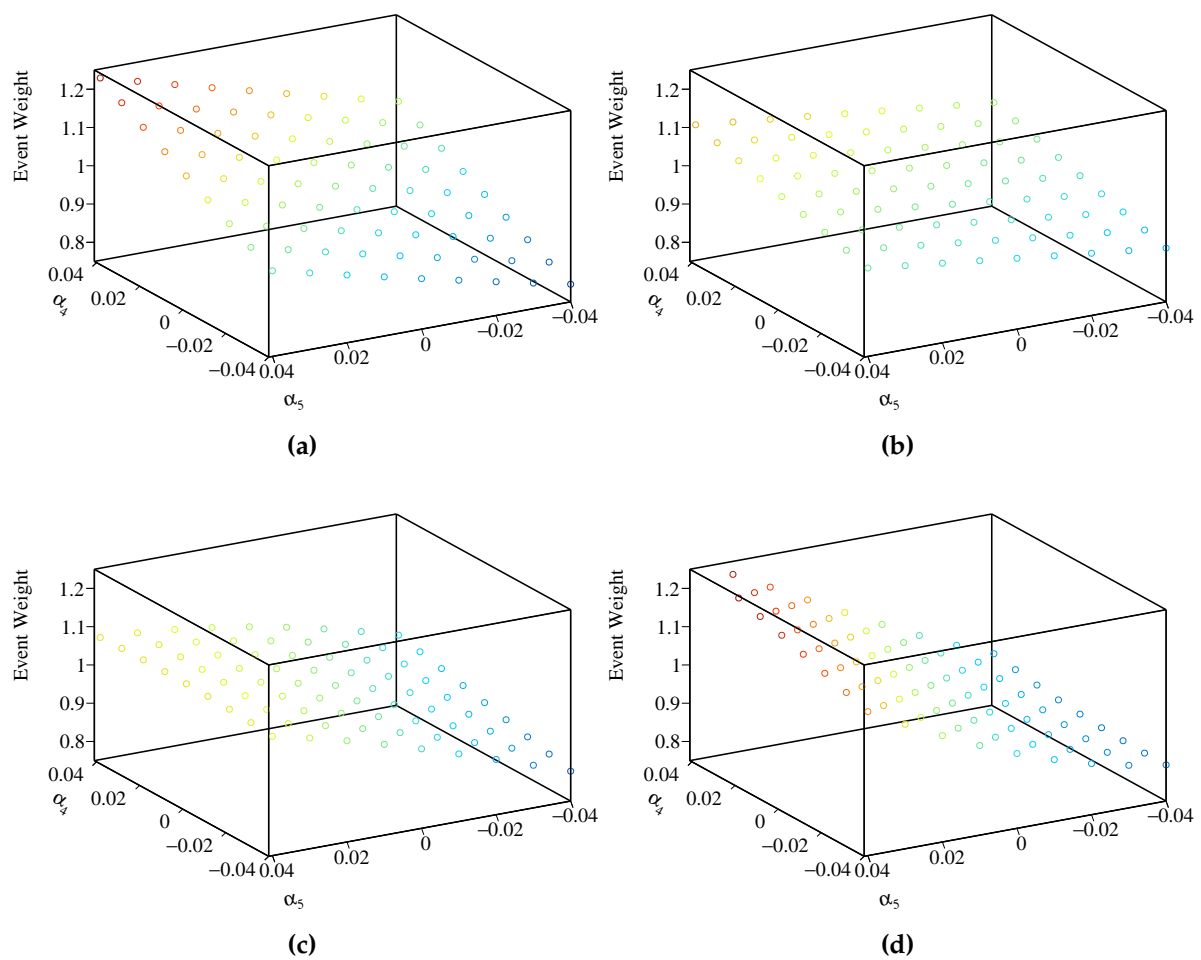


Figure 2.1.: A selection of plots showing how the event weight changes when varying the anomalous couplings α_4 and α_5 for 1.4 TeV $\nu\nu qq qq$ final state events.

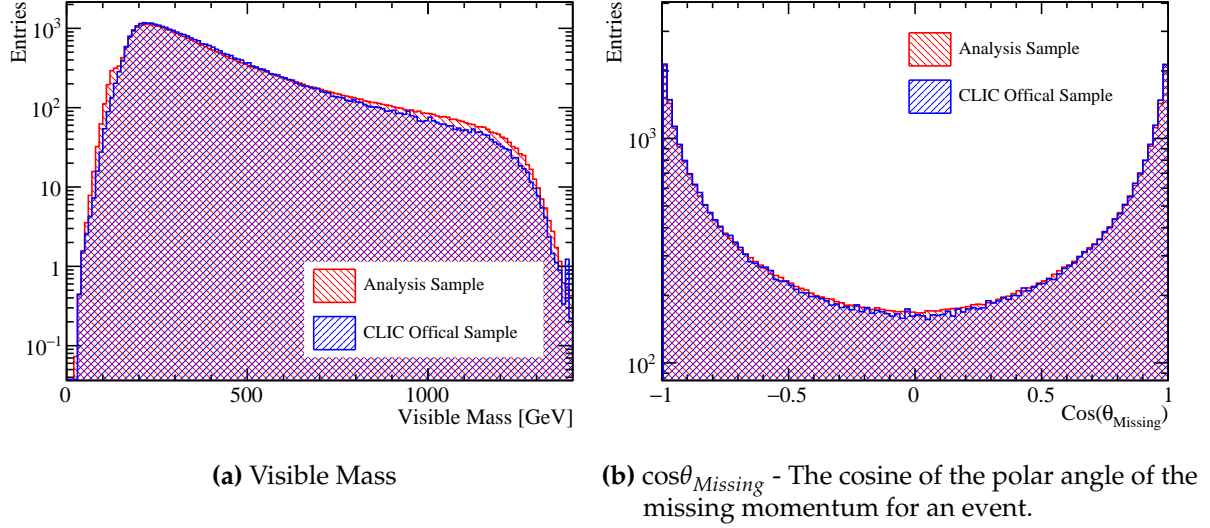


Figure 2.2.: Comparison of various distributions between samples used in this analysis and the official CLIC samples for the $\nu\nu qq qq$ final state at 1.4 TeV.

a function of α_4 and α_5 possible. An identical setup to that used for the production of official CLIC samples was used for the event generation, detector simulation and reconstruction. Mimicking this production chain made it possible to use the official CLIC samples for the background final states used in this analysis.

Several reconstructed level distributions were compared to the official CLIC samples and were found to be comparable to each other. A selection of these distributions is shown in figure 2.2.

In order to determine the event weights it was necessary to use the anomalous gauge coupling model in Whizard, which in turn enforces a unit CKM matrix. In the context of vector boson scattering this will restrict the hadronic decays of the W^- boson to $d\bar{u}$ and $s\bar{c}$, the W^+ boson to $u\bar{d}$ and $c\bar{s}$ and the Z boson to $u\bar{u}$, $d\bar{d}$, $s\bar{s}$, $c\bar{c}$ and $b\bar{b}$. In contrast the official CLIC samples use a non-unit CKM matrix, which gives rise to alternative hadronic decay modes for the W and Z bosons. When comparing the unit CKM matrix and the non-unit CKM $\nu\nu qq qq$ final state samples it was found that there were negligible differences in a variety of reconstructed level distributions, such as those found in figure 2.2. Furthermore, as flavour tagging information is not used in this analysis this difference was deemed insignificant.

Make 3 TeV Comparison <-

2.3. Simulation and Reconstruction

The CLIC_ILD detector [1] was simulated using MOKKA [10], a GEANT4 [2] wrapper providing detailed geometric descriptions of detector concepts for the linear collider. Events were reconstructed using MARLIN [5] a c++ framework designed for reconstruction at the linear collider. PandoraPFA [9, 15] is used to apply particle flow calorimetry to these samples and to produce PFOs that are used in this analysis.

Using the CLIC_ILD detector for this analysis provides access to the background samples created by the CLIC collaboration. The CLIC_ILD detector has a 60 layer scintillator-tungsten HCal in comparison to the 48 layer HCal found in the default ILD detector. The increase in thickness of the detector for the CLIC experiment is needed to compensate for the effects of leakage at the higher energies seen by the CLIC experiment in comparison to the ILC. Practically speaking the ILD and CLIC_ILD detectors are otherwise identical.

2.3.1. Experimental Conditions at CLIC

The CLIC experiment will operate in a unique environment in comparison to previous generations of lepton colliders and these must be properly accounted for in any analysis to get a measure of the true physics potential CLIC has to offer. The following aspects of the CLIC experiment present the largest challenges to the physics potential for the CLIC experiment:

- The high bunch charge density. The small beam size at the impact point produces very large electromagnetic fields that interact with the particles from the opposite beam causing them to radiate photons. This effect is known as beamstrahlung and it acts to reduce the collision energy of the e^+e^- pairs.
- Beam related backgrounds. Beamstrahlung photons can further interact through a number of different mechanisms each of which contribute to different background processes that must be accounted for. Dominant processes that cannot be easily vetoed include incoherent pair production of e^+e^- and $\gamma\gamma \rightarrow \text{Hadron}$.
- Fast readout technology is crucial. The CLIC bunch train consists of 312 bunches with a repetition rate of 50 Hz. Each bunch is separated by 0.5ns. As this is such a small separation it will be necessary to integrate over multiple bunch crossing

when reading out the detectors. This places tight constraints on all detector electrical readout speeds and time resolutions.

2.3.2. Beam-Related Backgrounds at CLIC

The primary sources of background for the CLIC experiment are as follows:

- e^+e^- pair creation from the interaction of a beamstrahlung photons with the electromagnetic field from the opposite beam. The different mechanisms for pair creation are coherent, incoherent and trident pairs are pair production. Coherent pair production occurs when a real beamstrahlung photon interacts with the electromagnetic field from the opposite beam, trident pair production occurs when a virtual beamstrahlung photon interacts with the electromagnetic field from the opposite beam and incoherent pair production occur when a real or virtual beamstrahlung photon interacts with the individual particles in the opposite beam.
- $\gamma\gamma \rightarrow \text{Hadron}$ from the interaction of real or virtual beamstrahlung photons with each other. Example Feynman diagrams for such processes is shown in figure ??.
- Beam halo muons that arise from inelastic collisions of the beam particles during collimation.

Each of these has to be properly addressed to get a true measure of the physics potential at CLIC. Coherent and trident pair production is not a dominant source of background as they are produced at low transverse momenta, as figure 2.3 shows, and a simple cut could veto these backgrounds. This is not the case for incoherent pair production of e^+e^- , which are dominant in the forward regions of the detector, and $\gamma\gamma \rightarrow \text{Hadron}$, which are dominant in the tracker and the calorimeters (with the exception of low radii in the calorimeter endcaps) [8, 13]. Beam halo muons prove not to be a dominant source of background either as, thanks to the unique topology of a muon passing through a detector it is possible to isolate them at PFO construction and remove them from further processing. A preliminary version of a processor designed for this purpose was implemented within PandoraPFA [8].

As $\gamma\gamma \rightarrow \text{Hadron}$ events deposit more energy than incoherent pair production [8], they are the most dominant background to consider. They are included into this analysis by overlaying $\gamma\gamma \rightarrow \text{Hadron}$ events onto the signal events. For each event

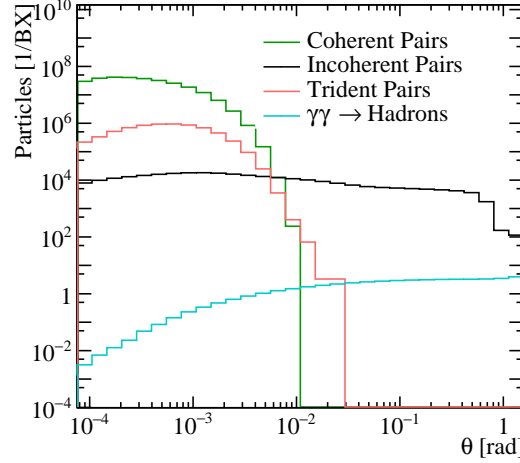


Figure 2.3.: Angular distribution of number of particles for beam induced backgrounds for CLIC at $\sqrt{s} = 3$ TeV. Taken from CLIC CDR.

the exact number of events overlaid is drawn from a Poisson distribution with a mean of 3.2(1.3) events per bunch crossing at 3(1.4) TeV. While incoherent pairs are still a source of background they will produce a second order effect in comparison to the $\gamma\gamma \rightarrow \text{Hadron}$ events.

The PFO choices described in section 2.6 are applied to veto PFOs that arise from the overlaid $\gamma\gamma \rightarrow \text{Hadron}$ events.

2.4. Analysis Processor and Jet Pairing

For both signal and background events the MarlinFastJet processor, a wrapper for the FastJet [4] process, is used to cluster the events into 4 jets. These are jets assumed to be from the hadronic decays of the bosons involved in the vector scattering process. These jets are paired up such that on the assumption that the correct pair arises when the invariant masses of the two pairs are closest together. The longitudinally invariant kt jet algorithm in exclusive modes is used for the jet clustering. This jet algorithm proceeds as follows:

- For each pair of particles i and j work out the kt distance and beam distance $d_{iB} = p_t^2$.

$$d_{ij} = \min(p_{ti}^2, p_{tj}^2) \Delta R_{ij}^2 / R^2 \quad (2.1)$$

where $\Delta R_{ij}^2 = (y_i - y_j)^2 + (\phi_i - \phi_j)^2$. p_t is the transverse momentum of the particle with respect to the beam axis, y_i is the rapidity of particle i and ϕ_i is the azimuthal angle of particle i . R is a configurable parameter that typically is of the order of 1.

- Find the minimum distance d_{\min} of all the k_t and beam distances. If the minima occurs for a k_t distance, merge particles i and j , summing their 4-momenta in the energy combination scheme (also configurable). If the beam distance is the minimum declare particle i to be apart of the "beam" jet and remove it from the list of particles and not included in the final output jets.
- Repeat until no particles are left or the requested number of jets have been created (or optionally apply a minimum d_{cut} where clustering stops, but here the event is forced into 4 jets).

An inclusive mode is available, but not applied here as the finally number of jets in the output varies and events need to be clustered into 4 jets for this analysis. Two other clustering modes were considered, but were found to be inappropriate for this analysis as is shown in figure 2.4. They were:

- The k_t algorithm for e+e colliders (or Durham algorithm) where $d_{ij} = 2\min(E_i^2, E_j^2)(1 - \cos\theta_{ij})$ and d_{iB} is not used. θ_{ij} is the opening angle of the particles. In the collinear limit this corresponds to the relative transverse momentum of the particles. Unlike the other algorithm choices this is not invariant to boosts along the beam direction as in theory for e+e colliders the collision should occur with no net 3 momentum, unlike hadron colliders where the events have a net 3-momentum. However, the presence of ISR and beam effects makes this algorithm inappropriate for CLIC. The major failure of this algorithm choice is the absence of d_{iB} as this associates too many background particles to jets when applied at CLIC.
- The Cambridge/Aachen jet algorithm where $d_{ij} = \Delta R_{ij}^2/R^2$ and $d_{iB} = 1$. This algorithm gave poor performance as it is based entirely on spacial information and does not account for the transverse momentum or energy of the particles being grouped. In essence this is a cone clustering algorithm with a cone radius defined through $\Delta R_{ij} = R$, which even for large R was found to throw away too much energy in the event to be useful for this analysis. This algorithm can be useful for events with small jets that are highly boosted, but in this case the jets are too large to be successfully merged.

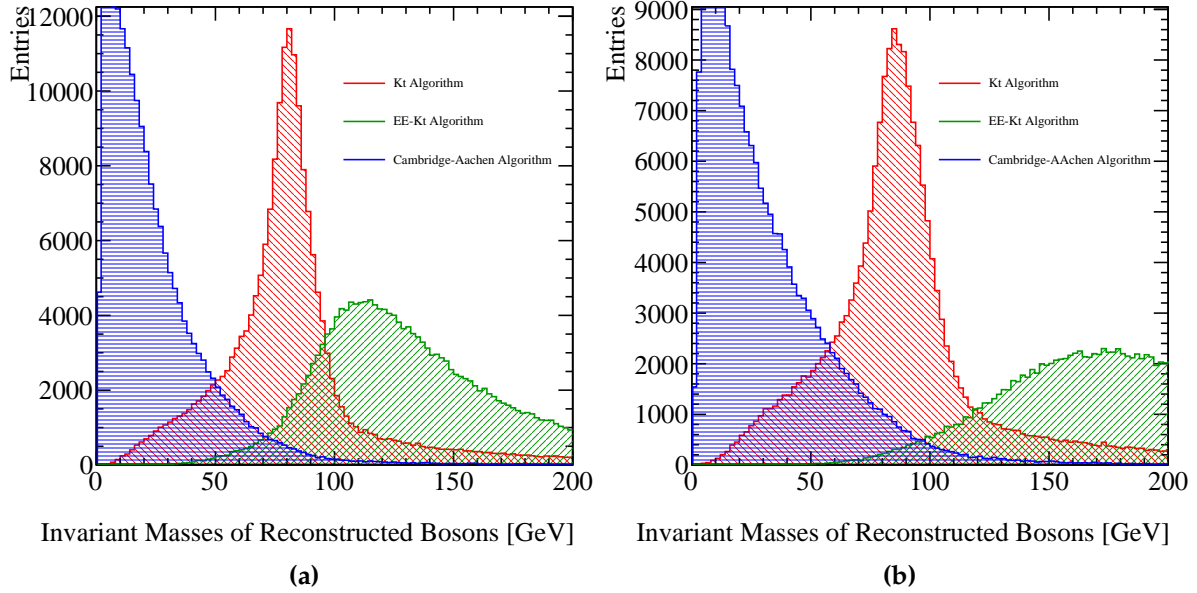


Figure 2.4.: Reconstructed masses for different choices of jet algorithm for 1.4 TeV and 3 TeV $\nu\nu qqqq$ events. These masses arise by forcing the reconstructed events into 4 jets and then pairing up the jets into pairs such that the reconstructed invariant masses of the pairs are closest to each other. These samples should be dominated by vector boson scattering involving pairs of W bosons and so it is expected that a peak at the W boson true mass should be observed. As this does not occur for the Cambridge-Aachen algorithm or the ee_kt algorithm they were deemed unsuitable for this analysis at both 1.4 and 3 TeV. In the case of the kt algorithm and the ee_kt algorithm an R parameter of 0.7 was used.

An isolated lepton finder is included in the analysis chain in an attempt to reject background events containing leptons. The LCFIPlus [14] processor is also run on these events once clustered into jets to produce a value for the B and C tag likelihood for a jet.

This information is available for background rejection rather than contributing to the sensitivity of the event to the anomalous couplings. The LCFIPlus vertex processor was trained using events of $e^+e^- \rightarrow Z\nu\nu \rightarrow q\bar{q}\nu\nu$ for $q = u, d, s, c, b$.

Finally, an analysis processor is run, which calculates a number of variables used downstream in the analysis. Included in these are:

- Number of PFOs in the jets and the paired up bosons.
- Number of charged PFOs in the jets and paired up bosons.
- Highest energy PFO: energy, momentum, transverse momentum, $\cos\theta$.
- Highest energy electron PFO: energy, momentum, transverse momentum, $\cos\theta$.
- Highest energy muon PFO: energy, momentum, transverse momentum, $\cos\theta$.
- Highest energy photon PFO: energy, momentum, transverse momentum, $\cos\theta$.
- (If in existence) Highest and second highest energy isolated lepton: energy, momentum, transverse momentum, $\cos\theta$.
- Bosons: energy, momentum, transverse momentum, $\cos\theta$.
- Invariant mass of the boson pair.
- Jets: energy, momentum, transverse momentum, $\cos\theta$.
- $\cos\theta$ Of the missing 3-momentum vector.
- Recoil mass.
- Invariant mass of the visible system.
- y_i, y_{i+1} . Jet clustering parameters ranging from $i = 0$ to 6.
- $\cos\theta_{jet}^*$. This is the opening angle of a pair of jets, assumed to be from a single boson, in the rest frame of the boson.

- $\cos\theta_{Boson}^*$. This is the opening angle of a pair of bosons, assumed to be from vector boson scattering, in the rest frame of the di-boson pair.
- Transverse momentum and energy of the event.
- Acolinearity of the jet pairs forming the bosons and the acolinearity of the boson pair.
- Principle thrust T and the thrust axes $\bar{\mathbf{n}}$. Note $\bar{\mathbf{n}}$ is a unit vector. These are defined by the following equation

$$T = \max_{\bar{\mathbf{n}}} \left(\frac{\sum_i \mathbf{p}_i \cdot \bar{\mathbf{n}}}{\sum_i |\mathbf{p}_i|^2} \right) \quad (2.2)$$

- The major and minor thrust values. These are defined with respect to the thrust axes $\bar{\mathbf{n}}$ in the following way:

$$T = \max_{\bar{\mathbf{n}}_{major}} \left(\frac{\sum_i \mathbf{p}_i \cdot \bar{\mathbf{n}}_{major}}{\sum_i |\mathbf{p}_i|^2} \right) \quad (2.3)$$

where $\bar{\mathbf{n}}_{major} \cdot \bar{\mathbf{n}} = 0$. Similarly the minor thrust value is defined as

$$T = \frac{\sum_i \mathbf{p}_i \cdot \bar{\mathbf{n}}_{minor}}{\sum_i |\mathbf{p}_i|^2} \quad (2.4)$$

where $\bar{\mathbf{n}}_{minor} \cdot \bar{\mathbf{n}} = \bar{\mathbf{n}}_{minor} \cdot \bar{\mathbf{n}}_{major} = 0$

- Sphericity. This is defined using the sphericity tensor S^{ab} defined as:

$$S^{ab} = \frac{\sum_i p_i^\alpha p_j^\alpha}{\sum_{i,\alpha=1,2,3} |p_i^\alpha|^2} \quad (2.5)$$

Where p_i are the components of the momenta of particle i in the frame of the detector and the sum runs over all particles in the event. Sphericity is defined as $S = \frac{3}{2}(\lambda_2 + \lambda_3)$, where λ_i are the eigenvalues of the sphericity tensor defined such $\lambda_1 \geq \lambda_2 \geq \lambda_3$. This provides a measure of how spherical the reconstructed event topology is with isotropic events having $S \approx 1$, while two jet events have $S \approx 0$. (Also $\lambda_1 + \lambda_2 + \lambda_3 = 1$.)

- Aplanarity. Aplanarity is defined as $\frac{3}{2}\lambda_3$ where λ_3 is an eigenvalue of the sphericity tensor. This provides a measure of whether an event is linear or planar.

- B and C tag values for the jets, the min and max B and C tag values for the bosons.

Alongside these variables, for the $\nu\nu qqqq$ final state a number of Monte-Carlo variables are calculated for informative purposes and are not used in the analysis. These include:

- The quark and neutrino 4 momenta.
- Invariant mass of boson pair using MC pairing and MC energy.
- Invariant mass of boson pair using MC pairing and reconstructed jet energy.

2.5. Methodology for Fitting

It is necessary to discuss the fitting procedure in this analysis as the optimisation of the jet algorithms relies on this methodology. In this section only the signal events are considered to determine the underlying sensitivity of the CLIC detector to the anomalous couplings. This decision was made to save analysis of the large number of background samples in the optimisation of the jet reconstruction algorithms, while still optimising the algorithm on the physics of interest.

2.5.1. Choice of Fitting Distribution

The sensitivity of CLIC to the anomalous gauge couplings is determined through the use of a χ^2 fit to the distribution of $\cos\theta_{jets}^*$ where θ_{jets}^* is the angle between the two jets produced from the hadronic decay of the W/Z boson in the rest frame of that boson. The distribution of $\cos\theta_{jets}^*$ proved to be sensitive to the anomalous gauge couplings as shown in figure 2.5.

Another distribution considered for the sensitivity study was $\cos\theta_{Bosons}^*$ where θ_{Bosons}^* is the angle between the two bosons produced in vector boson scattering in the rest frame of the boson pair. This distribution was found to be less sensitive to the anomalous gauge couplings than $\cos\theta_{jets}^*$, which can be seen when comparing figures 2.5 and 2.6, and so was not considered for the rest of this study. Furthermore, it was found that a two dimensional χ^2 fit produced by combining $\cos\theta_{jets}^*$ and $\cos\theta_{Bosons}^*$ did not improve the sensitivity significantly in comparison to $\cos\theta_{jets}^*$.

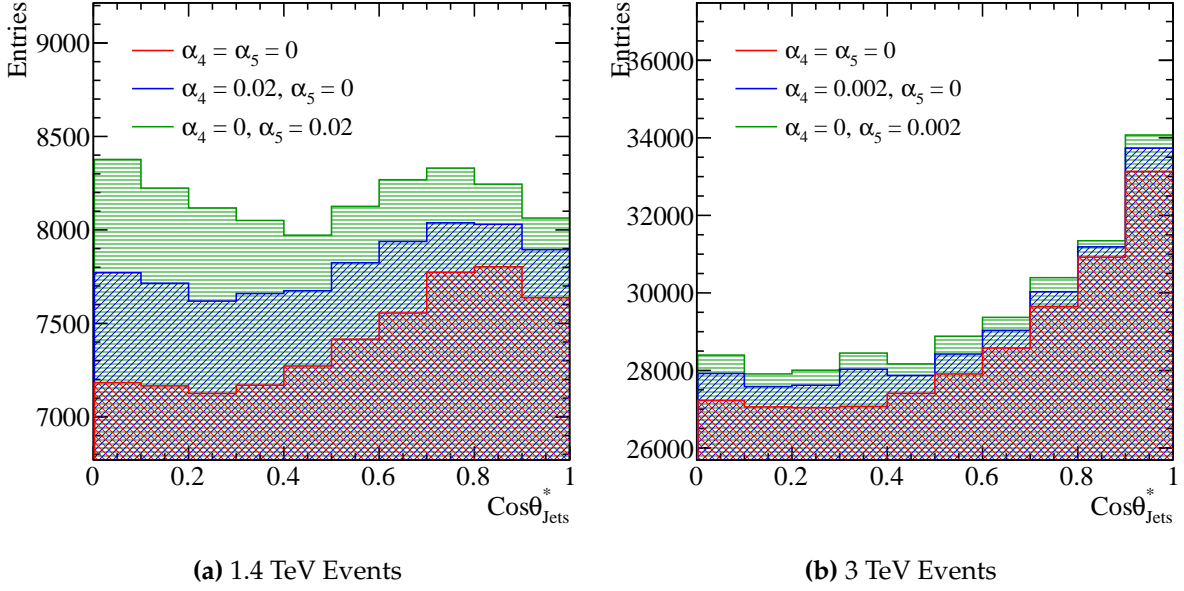


Figure 2.5.: Sensitivity of $\cos\theta_{jets}^*$ to anomalous couplings at 1.4 and 3 TeV. The jet algorithm used for this example was the longitudinally invariant kt algorithm with an R parameter of 0.7. This sample corresponds to pure signal of hadronic decays in vector boson scattering i.e. $\nu\nu qqqq$.

The $\cos\theta_{jets}^*$ variable was binned in histograms of 10 bins before begin converted into a value of χ^2 . This binning was selected to maximise the number of bins in the distribution, while minimising the effect of large bin by bin fluctuations arising from individual events with large event weights.

2.5.2. Event Weight Impact on Fitting Distribution

At 1.4 TeV event weights were produced from Whizard stepping along α_4 and α_5 in steps of 0.01 ranging from -0.07 to 0.07 as shown in figure 2.4, however, to produce a smooth χ^2 contour much finer sampling is needed. While it is feasible to generate new event weights in Whizard for any pair of α_4 and α_5 it is time consuming making it impractical for this analysis. To overcome this difficulty bicubic interpolation is applied between these points to allow for the extract of event weights anywhere within the range -0.05 to 0.05. As figure 2.7 shows the interpolated surface proves to be a good fit to the data produced from the generator in that it is smooth and continuous.

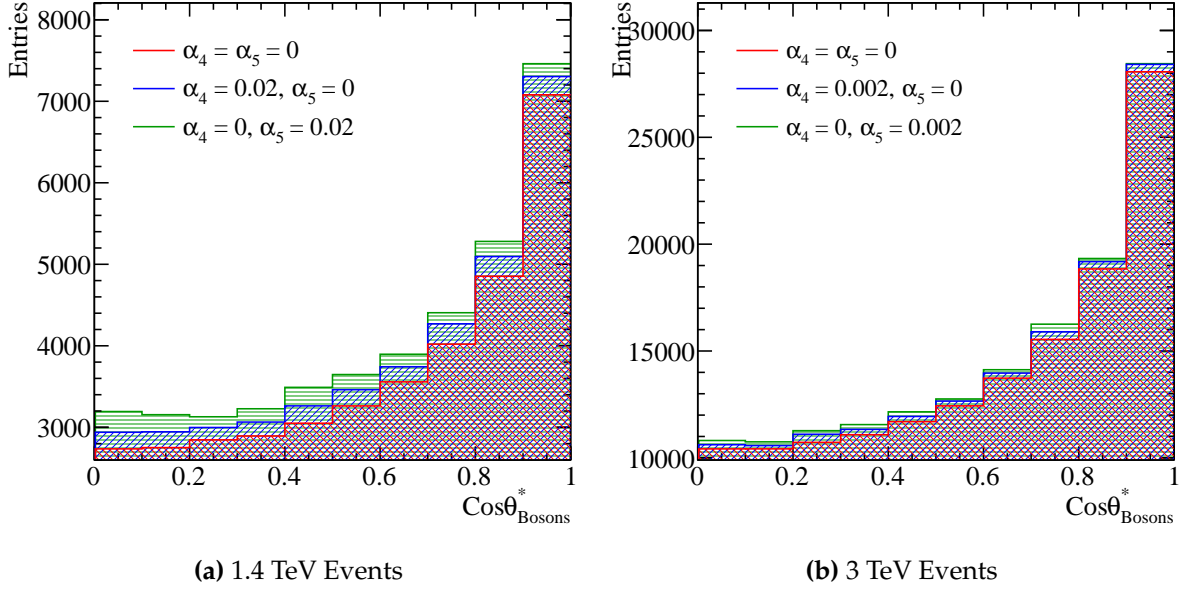


Figure 2.6.: Sensitivity of $\cos\theta_{Bosons}^*$ to anomalous couplings at 1.4 and 3 TeV. The jet algorithm used for this example was the longitudinally invariant kt algorithm with an R parameter of 0.7. This sample corresponds to pure signal of hadronic decays in vector boson scattering i.e. $\nu\nu qqqq$.

Similarly at 3 TeV the same procedure was used but stepping occurs in steps of 0.001 ranging from -0.007 to 0.007 in both α_4 and α_5 . These ranges proved to be sufficient for the contours of interest for the CLIC sensitivity analysis at this energy.

2.5.3. Analysis of Fitting Distribution

Using these interpolated surfaces for the event weights, distribution of $\cos\theta_{jets}^*$ were produced stepping across α_4 and α_5 in steps of 0.0001 at 1.4 TeV and 0.00001 at 3 TeV. Each distribution was converted into a value of χ^2 using the following formula:

$$\chi^2 = \sum_i \frac{(O_i - E_i)^2}{E_i} \quad (2.6)$$

where O_i is the observed bin content for bin i in the distribution with non-zero α_4 and α_5 and E_i is the expected bin content for bin i in the distribution with zero α_4 and α_5 i.e. the standard model expected value.

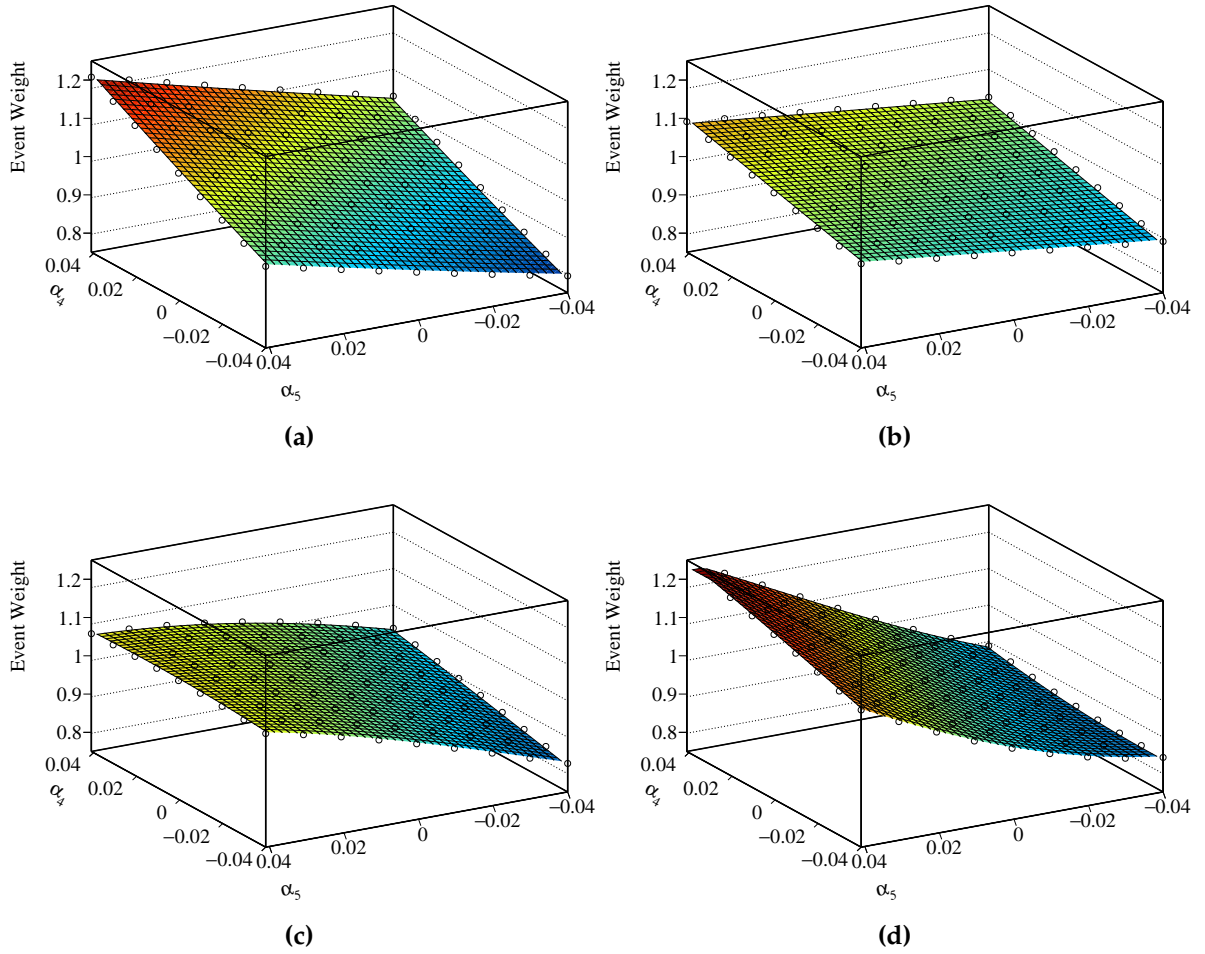


Figure 2.7.: A selection of plots showing how the event weight changes when varying the anomalous couplings α_4 and α_5 for 1.4TeV $\nu\nu qqqq$ final state events. The hollow circles show the event weight produced from the generator while the surface shown is found using bicubic interpolation between those points.

Confidence limits indicate the probability of measuring a given value of χ^2 in the α_4 and α_5 space. The confidence limits used in subsequent sections, 68%, 90% and 99% are defined using constant χ^2 contours of 2.28, 4.61 and 9.21, which arise from the integral of the two dimensional χ^2 function.

It is useful to reduce these distributions to sensitivities to the individual parameters α_4 and α_5 independently. This is done by projecting out either the $\alpha_4 = 0$ or $\alpha_5 = 0$ one dimensional χ^2 distribution from the two dimensional χ^2 distribution. Using these one dimensional plots it is possible to extract the sensitivity to an individual parameters using confidence limits arising from the integral of the two dimensional χ^2 function i.e. 68% confidence limit occurs for $\chi^2 = 0.989$. In subsequent chapters these are the sensitivities quoted for individual anomalous gauge coupling parameters.

2.6. Optimisation of Jet Reconstruction

The jet algorithm used for this analysis is the longitudinally invariant kt algorithm as described in section 2.4. The parameter choices under consideration for optimisation are the R parameter, used in the kt algorithm definition, used and the PFO selection.

A number of cuts [9] are applied to the transverse momenta and the time of the PFOs produced by PandoraPFA to reduce the PFOs into a subset that are believed to originate from the desired interaction in an attempt to veto the overlaid $\gamma\gamma \rightarrow \text{Hadron}$ background events. Different options for these cuts give rise to the tight, default and loose selected PFOs that are considered in this optimisation.

2.6.1. 1.4 TeV Optimal Jet Reconstruction

At 1.4 TeV the optimal sensitivity is achieved for either loose selected PFOs with an R parameter of 0.7 or default selected PFOs with an R parameter of 0.9 as can be seen from tables 2.3 and 2.4. As a tie breaker between these options the separation power, the fraction of events misidentified as either arising from a WW pair or a ZZ pair, was considered. Again performance was similar, but there was a slight preference towards the use of selected PFOs and an R parameter of 0.9. While not used in the primary analysis the separation of samples into WW and ZZ events is important for an extension analysis found in section BLAH.

The optimal contours can be found in figure 2.8a and the optimal 1D plot used to produce the errors references in the tables 2.3 and 2.4 can be found in figures 2.8b and 2.8c respectively. All other contours and plots for this optimisation can be found in the appendices. There are minimal performance differences between the various jet algorithm configurations at 1.4 TeV.

PFO Selection	Tight Selected PFOs	Selected PFOs	Loose Selected PFOs
R Parameter			
0.7	$-0.0039 + 0.0050$	$-0.0038 + 0.0050$	$-0.0037 + 0.0046$
0.9	$-0.0041 + 0.0051$	$-0.0038 + 0.0046$	$-0.0038 + 0.0048$
1.1	$-0.0041 + 0.0051$	$-0.0039 + 0.0050$	$-0.0040 + 0.0050$

Table 2.3.: Precision on measurement of α_4 at 1.4 TeV for different jet reconstruction parameters considering pure signal and applying a χ^2 fit to $\cos\theta_{jets}^*$.

PFO Selection	Tight Selected PFOs	Selected PFOs	Loose Selected PFOs
R Parameter			
0.7	$-0.0027 + 0.0031$	$-0.0027 + 0.0032$	$-0.0025 + 0.0030$
0.9	$-0.0028 + 0.0032$	$-0.0026 + 0.0030$	$-0.0026 + 0.0030$
1.1	$-0.0028 + 0.0032$	$-0.0027 + 0.0032$	$-0.0028 + 0.0031$

Table 2.4.: Precision on measurement of α_5 at 1.4 TeV for different jet reconstruction parameters considering pure signal and applying a χ^2 fit to $\cos\theta_{jets}^*$.

2.6.2. 3 TeV Optimal Jet Reconstruction

At 3 TeV the optimal sensitivity for the reconstructions considered is achieved for tight selected PFOs with an R parameter of 1.1 as can be seen from tables 2.5 and 2.6. The optimal contours can be found in figure 2.9a and the optimal 1D plot used to produce the errors references in the tables 2.5 and 2.6 can be found in figures 2.9b and 2.9c respectively. All other contours and plots for this optimisation can be found in the appendices.

The gains in optimising the jet algorithm at 3 TeV are larger than those found at 1.4 TeV. The preference for the tight selected PFOs is to be expected as this configuration

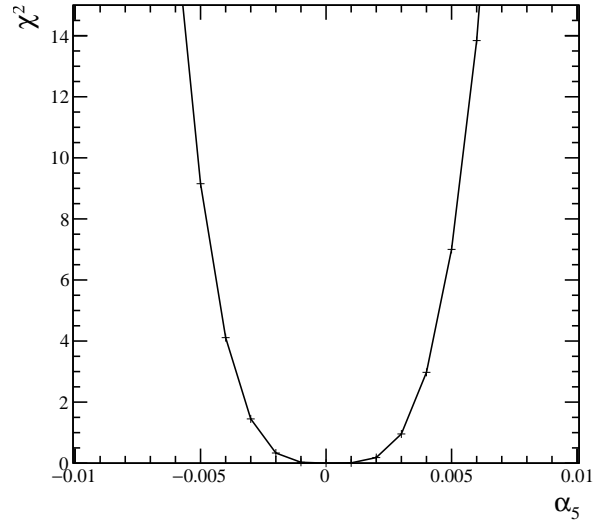
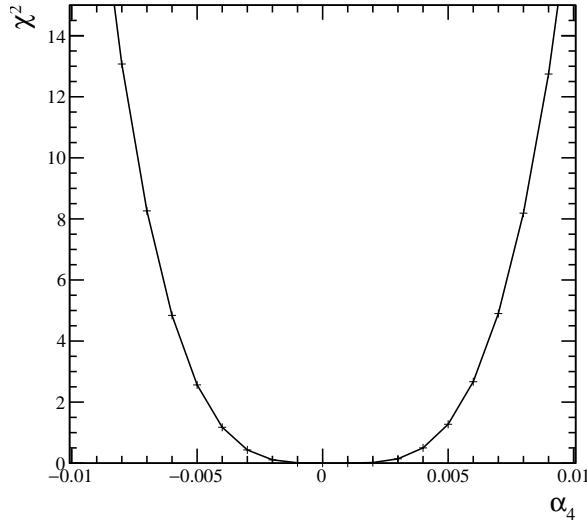
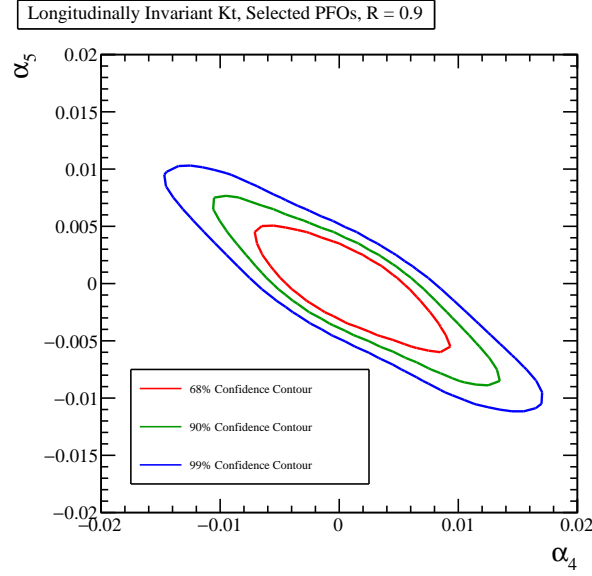


Figure 2.8.: χ^2 sensitivity distributions for the $qqqq\nu\nu$ final state arising from a fit to $\cos\theta_{\text{jets}}^*$ at 1.4 TeV for the optimal jet reconstruction parameters.

minimises the effect of beam induced backgrounds, which are more prominent at higher energies.

PFO Selection R Parameter	Tight Selected PFOs	Selected PFOs	Loose Selected PFOs
0.7	$-0.000529 + 0.000525$	$-0.000510 + 0.000507$	$-0.000547 + 0.000555$
0.9	$-0.000566 + 0.000555$	$-0.000539 + 0.000520$	$-0.000568 + 0.000553$
1.1	$-0.000472 + 0.000472$	$-0.000508 + 0.000492$	$-0.000504 + 0.000489$

Table 2.5.: Precision on measurement of α_4 at 3 TeV for different jet reconstruction parameters considering pure signal and applying a χ^2 fit to $\cos\theta_{jets}^*$.

PFO Selection R Parameter	Tight Selected PFOs	Selected PFOs	Loose Selected PFOs
0.7	$-0.000392 + 0.000369$	$-0.000355 + 0.000348$	$-0.000356 + 0.000348$
0.9	$-0.000394 + 0.000365$	$-0.000391 + 0.000361$	$-0.000395 + 0.000368$
1.1	$-0.000350 + 0.000337$	$-0.000374 + 0.000354$	$-0.000352 + 0.000336$

Table 2.6.: Precision on measurement of α_5 at 3 TeV for different jet reconstruction parameters considering pure signal and applying a χ^2 fit to $\cos\theta_{jets}^*$.

2.7. Event Selection

As discussed earlier the signal events for this analysis contain the $\nu\nu qqqq$ final state. The processes to be considered in this analysis alongside the signal are events that would topologically look similar to signal in the detector. This includes events that could be confused with 4 jet events with missing energy, while excluding those events with large numbers of high energy leptons that could be vetoed easily during the analysis stage. In full the list includes:

Equivalent Photon Approximation (EPA) processes model the electromagnetic field of a charged particle as virtual photons. BS (beamstrahlung) processes involve photons that have been radiated from incoming charged particles due to interactions with the electromagnetic field of the opposite beam. The energy spectrum of the incoming

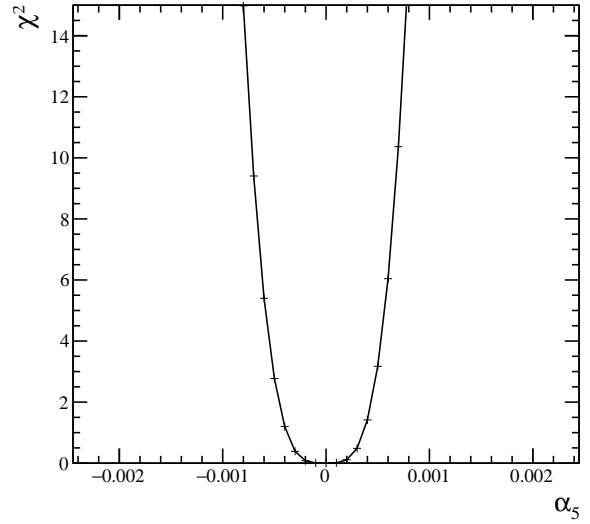
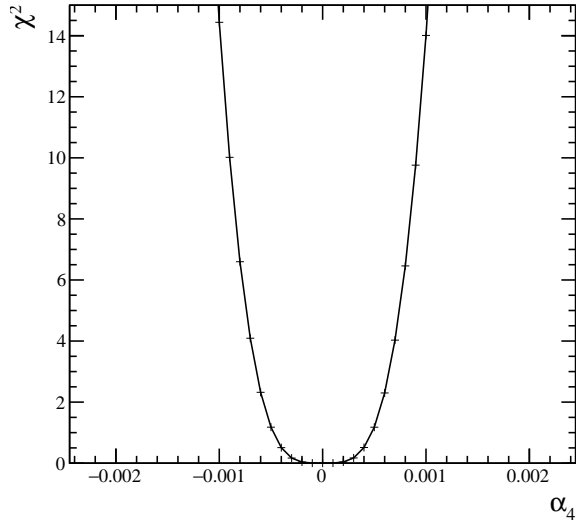
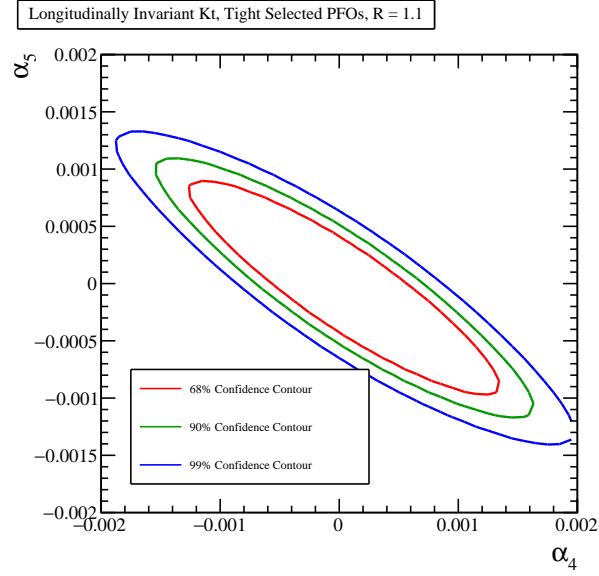


Figure 2.9.: χ^2 sensitivity distributions for the $qqqq\nu\nu$ final state arising from a fit to $\cos\theta_{\text{jets}}^*$ at 3 TeV for the optimal jet reconstruction parameters.

Final State	Cross Section 1.4 TeV [fb]	Cross Section 3 TeV [fb]
$e^+e^- \rightarrow \nu\nu qqqq$	24.7	71.5
$e^+e^- \rightarrow l\nu qqqq$	110.4	106.6
$e^+e^- \rightarrow ll qqqq$	62.1	169.3
$e^+e^- \rightarrow qqqq$	1245.1	546.5
$e^+e^- \rightarrow \nu\nu qq$	787.7	1317.5
$e^+e^- \rightarrow l\nu qq$	4309.7	5560.9
$e^+e^- \rightarrow ll qq$	2725.8	3319.6
$e^+e^- \rightarrow qq$	4009.5	2948.9
$\gamma_{\text{EPA}}e^- \rightarrow qqqqe^-$	287.1	287.8
$\gamma_{\text{BS}}e^- \rightarrow qqqqe^-$	1160.7	1268.6
$e^+\gamma_{\text{EPA}} \rightarrow qqqqe^+$	286.9	287.8
$e^+\gamma_{\text{BS}} \rightarrow qqqqe^+$	1156.3	1267.3
$\gamma_{\text{EPA}}e^- \rightarrow qqqq\nu$	32.6	54.2
$\gamma_{\text{BS}}e^- \rightarrow qqqq\nu$	136.9	262.5
$e^+\gamma_{\text{EPA}} \rightarrow qqqq\nu$	32.6	54.2
$e^+\gamma_{\text{BS}} \rightarrow qqqq\nu$	136.4	262.3
$\gamma_{\text{EPA}}\gamma_{\text{EPA}} \rightarrow qqqq$	753.0	402.7
$\gamma_{\text{EPA}}\gamma_{\text{BS}} \rightarrow qqqq$	4034.8	2423.1
$\gamma_{\text{BS}}\gamma_{\text{EPA}} \rightarrow qqqq$	4018.7	2420.6
$\gamma_{\text{BS}}\gamma_{\text{BS}} \rightarrow qqqq$	21406.2	13050.3

Table 2.7.: Cross sections of signal and background processes at 1.4 and 3 TeV. In the above table $q \in u, \bar{u}, d, \bar{d}, s, \bar{s}, c, \bar{c}, b$ or \bar{b} while $l \in e^\pm, \mu^\pm$ or τ^\pm and $\nu \in \nu_e, \nu_\mu$ and ν_τ . The subscript EPA or BS for the incoming photons indicate whether the photon is generated from the equivalent photon approximation or beamstrahlung.

particles for CLIC at the relevant operating energy is used to model the energy of these incoming photons. Included in this study are photon-photon interactions from photons appearing from the EPA and beamstrahlung processes.

2.7.1. Pre Selection - 1.4 TeV

The primary selection of the $\nu\nu qqqq$ signal will be done using a multivariate analysis, however, in an attempt to veto trivial backgrounds a simple cut based preselection is applied. Cuts are applied to the transverse momentum, invariant mass of the visible

system and the number of isolated leptons. The raw distributions of these variables is shown in figure 2.10. Based on these distributions the following cuts were applied:

- Transverse momentum > 100 GeV. This cut is effective due to the presence of missing energy in the form of neutrinos in the signal final state.
- Visible mass of the system > 200 GeV. This cut is effective for accounting for the missing energy of the neutrinos in the final state along the longitudinal direction of the detector instead.
- Number of isolated leptons $= 0$. This cut vetoes a large number of events with leptons in the final state. The effect of these preselection cuts can be found in table 1.3. While a large fraction of the signal events are lost through these cuts, particularly the transverse momentum cuts, a much large fraction of background events are removed justifying the cut.

The event numbers for the signal and background are shown in table 2.8 as these cuts are cumulatively applied. These numbers are normalised to the correct luminosity for CLIC running at 1.4 TeV. As is expected the large transverse momentum cut removes practically all backgrounds containing no missing energy. The invariant mass cut removes significant fractions of two quark and missing energy events. Finally, the isolated lepton finder cut removes backgrounds containing visible leptonic final states.

2.7.2. MVA - 1.4 TeV

A multivariate analysis was applied to the data set to refine the selection using the TMVA toolkit [6]. The following variables were used for training the TMVA selection.

- Number of PFOs in the event.
- Highest energy PFO type.
- Transverse momentum of the event.
- $\cos\theta_{Missing}$. The cosine of the polar angle of the missing momentum.
- $\cos\theta_{Highest\ Energy\ Track}$. The cosine of the polar angle of the track with the largest momentum.
- y_i, y_{i+1} . Jet clustering parameters ranging from $i = 0$ to 6.

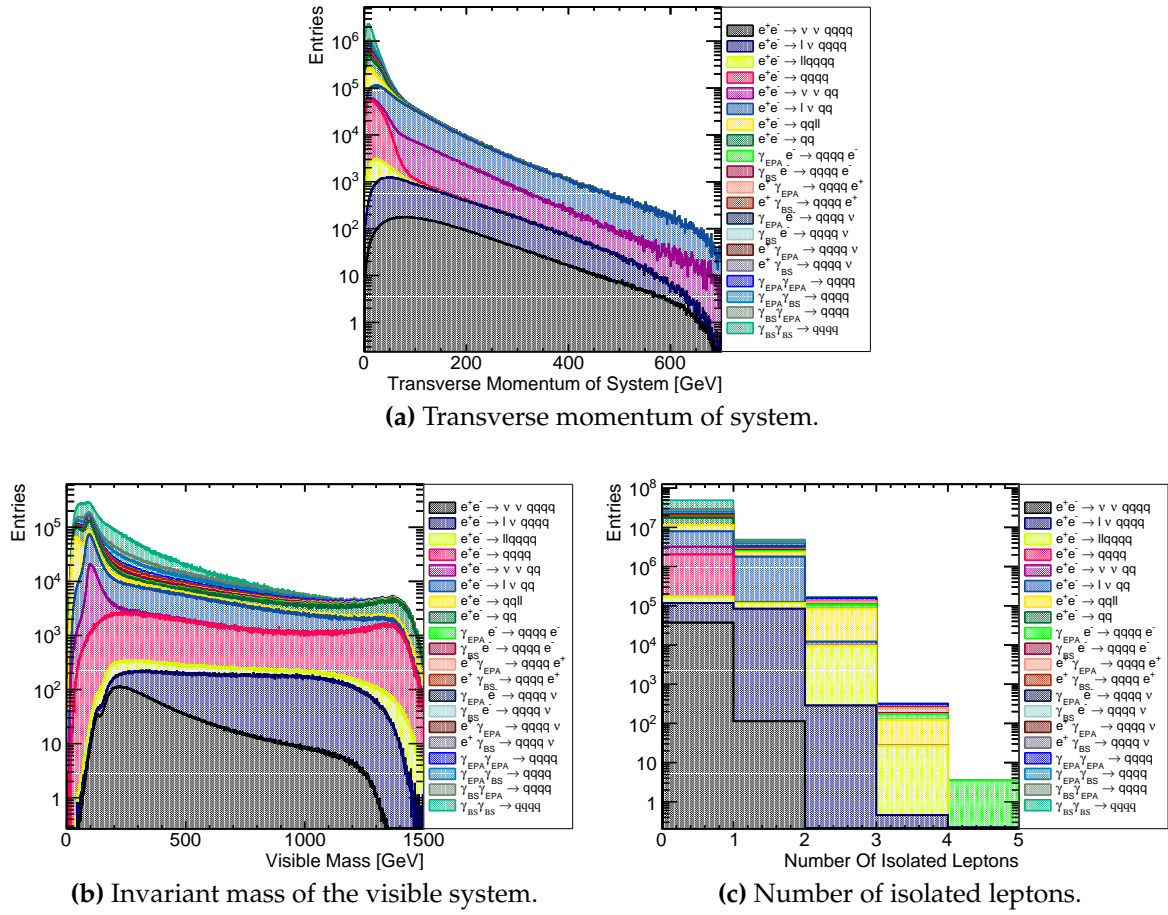


Figure 2.10.: Distribution of variables cut on in the preselection at 1.4 TeV.

Final State	Raw Event Numbers	$p_T > 100$ GeV	$p_T > 100$ GeV & $M_{\text{Vis}} > 200$ GeV	$p_T > 100$ GeV & $M_{\text{Vis}} > 200$ GeV & $N_{\text{Isolated Leptons}} = 0$
$e^+e^- \rightarrow \nu\nu qqqq$	37,050	23,800	21,080	21,020
$e^+e^- \rightarrow l\nu qqqq$	165,600	81,620	80,840	42,410
$e^+e^- \rightarrow ll qqqq$	93,150	1,151	1,140	700
$e^+e^- \rightarrow qq qq$	1,868,000	6,487	6,467	6,445
$e^+e^- \rightarrow \nu\nu qq$	1,181,000	514,100	50,260	50,150
$e^+e^- \rightarrow l\nu qq$	6,464,000	2,003,000	1,259,000	567,600
$e^+e^- \rightarrow ll qq$	4,088,000	7,754	7,351	5,643
$e^+e^- \rightarrow qq$	6,011,000	34,610	34,130	34,070
$\gamma_{\text{EPA}}e^- \rightarrow qq qq e^-$	430,600	2,463	2,446	865
$\gamma_{\text{BS}}e^- \rightarrow qq qq e^-$	1,306,000	1,382	1,340	1,002
$e^+\gamma_{\text{EPA}} \rightarrow qq qq e^+$	430,300	2,846	2,823	1,121
$e^+\gamma_{\text{BS}} \rightarrow qq qq e^+$	1,301,000	654	643	469
$\gamma_{\text{EPA}}e^- \rightarrow qq qq \nu$	48,890	17,450	13,490	8,852
$\gamma_{\text{BS}}e^- \rightarrow qq qq \nu$	154,000	56,380	36,350	35,900
$e^+\gamma_{\text{EPA}} \rightarrow qq qq \nu$	48,890	17,520	13,550	8,928
$e^+\gamma_{\text{BS}} \rightarrow qq qq \nu$	153,400	56,280	36,340	35,900
$\gamma_{\text{EPA}}\gamma_{\text{EPA}} \rightarrow qq qq$	1,129,000	3,160	3,079	1,563
$\gamma_{\text{EPA}}\gamma_{\text{BS}} \rightarrow qq qq$	4,539,000	5,325	5,270	3,987
$\gamma_{\text{BS}}\gamma_{\text{EPA}} \rightarrow qq qq$	4,521,000	3,810	3,730	2,318
$\gamma_{\text{BS}}\gamma_{\text{BS}} \rightarrow qq qq$	20,550,000	2,445	2,445	1,673

Table 2.8.: Number of events passing the various cuts applied in the preselection at 1.4TeV. Event numbers are normalised to the correct luminosity for CLIC at 1.4 TeV. p_T is the transverse momentum of the event, M_{Vis} is the visible mass and $N_{\text{Isolated Leptons}}$ is the number of isolated leptons in the event. In the above table $q \in u, \bar{u}, d, \bar{d}, s, \bar{s}, c, \bar{c}, b, \bar{b}$ while $l \in e^\pm, \mu^\pm$ or τ^\pm and $\nu \in \nu_e, \nu_\mu$ and ν_τ . The subscript EPA or BS for the incoming photons indicate whether the photon is generated from the equivalent photon approximation or beamstrahlung.

- Principle thrust, sphericity and aplanarity as defined in section BLAH.
- Energy of the highest energy electron in the event.
- Energy of the highest energy PFO in the event.
- Energy of the reconstructed bosons.

- Acolinearity of the reconstructed boson pair.
- Invariant mass of the reconstructed bosons.
- Acolinearity of the jets forming the reconstructed bosons.

It was found that the best MVA algorithm for both performance and speed was the booted decision tree (BDT) when comparing different methods using the default settings. Add plot here.

The BDT was further optimised by varying the number of trees used, the depth of the trees and the number of cuts applied. The results shown in the rest of this section use the optimal configuration. For the optimal BDT configuration a significance of $S/\sqrt{(S+B)} = 53.6$ was obtained.

The event numbers passing the BDT cut can be found in table 2.9. The performance of the BDT is shown in figure 2.11, which shows the change in the distribution of the the invariant mass of the reconstructed bosons as the MVA is applied. As expected the dominant background processes after the MVA is applied are those that will look identical to the visible signal process i.e. $qqqq$ and missing energy. Two smaller sources of background that pass the MVA exists, those where two jets and missing energy are confused as four jets and missing energy and those where a lepton is not properly reconstructed and the events look like four jets and missing energy.

The summary of the selection procedure is given in table 2.10.

2.7.3. Pre Selection - 3 TeV

2.7.4. MVA - 3 TeV

2.8. Results

2.8.1. 1.4 TeV

The sensitivity of the CLIC experiment to the anomalous gauge couplings α_4 and α_5 at 1.4 TeV is shown in figure 2.12a. This result shows the sensitivity after the application

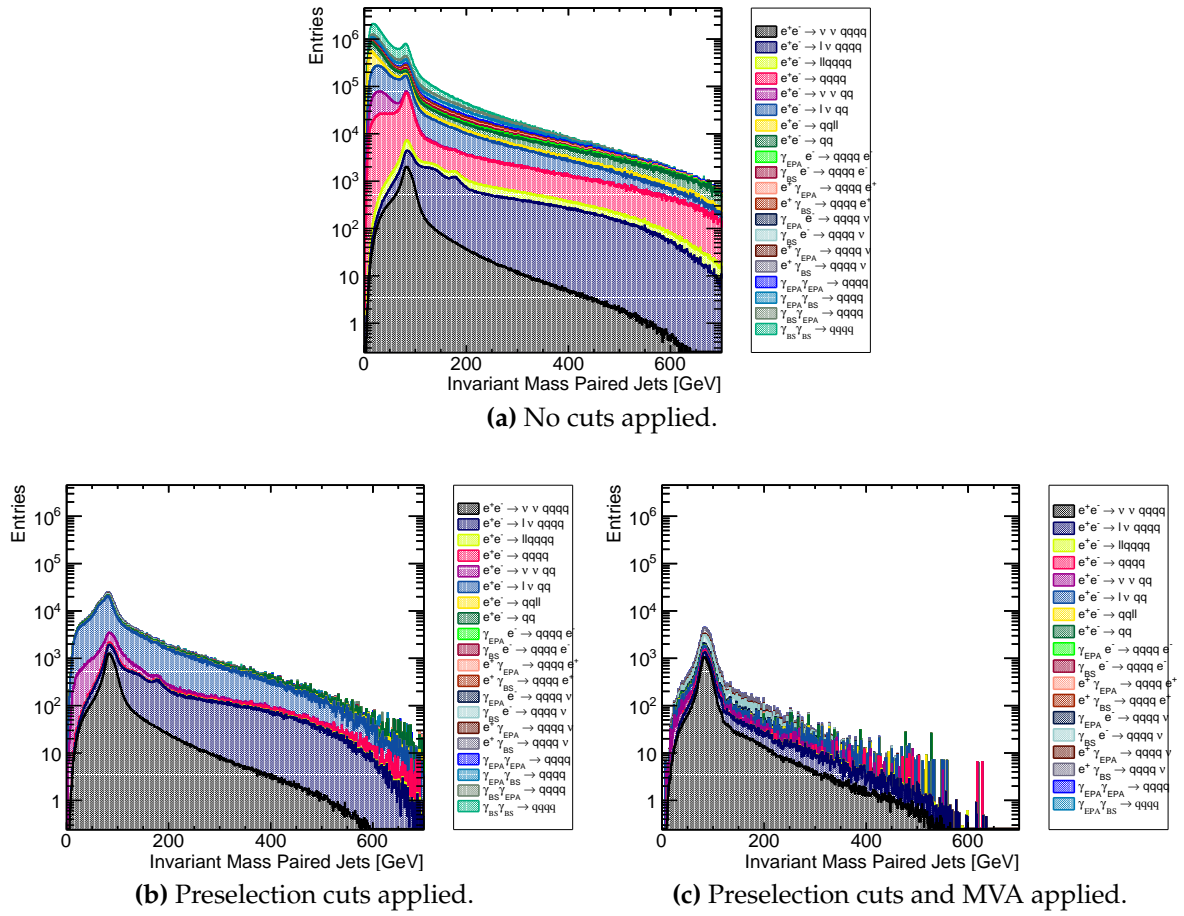
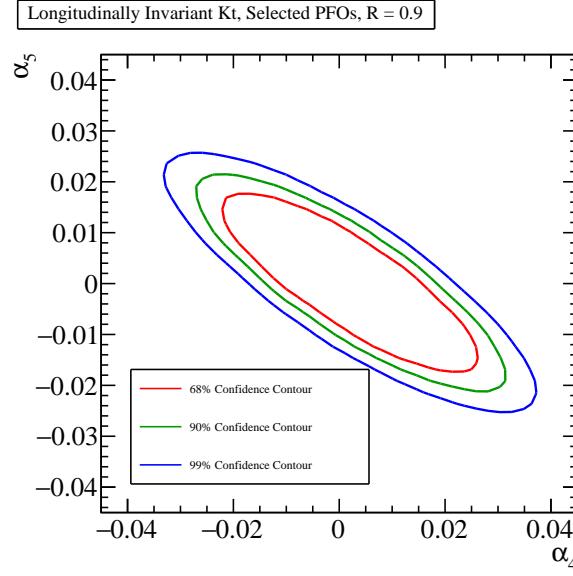


Figure 2.11.: Impact of preselection and MVA on the reconstructed invariant mass of the bosons arising from jet pairing at 1.4 TeV.

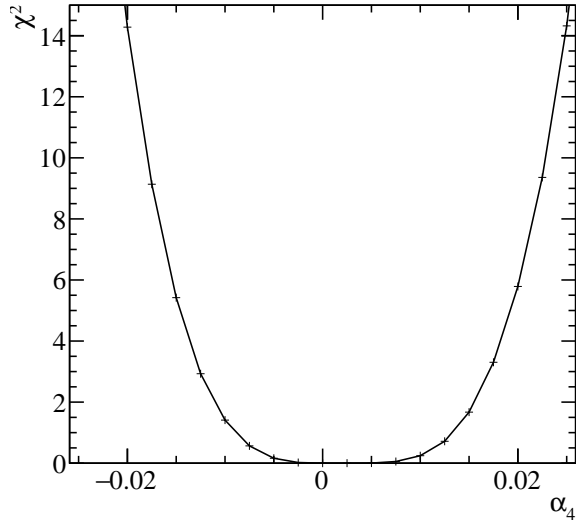
Final State	Raw Event Numbers	Post MVA Selection Numbers
$e^+e^- \rightarrow \nu\nu qqqq$	37,050	14,770
$e^+e^- \rightarrow l\nu qqqq$	165,600	6,159
$e^+e^- \rightarrow ll qqqq$	93,150	80
$e^+e^- \rightarrow qqqq$	1,867,631	1,264
$e^+e^- \rightarrow \nu\nu qq$	1,181,218	3,286
$e^+e^- \rightarrow l\nu qq$	6,463,852	6,262
$e^+e^- \rightarrow ll qq$	4,088,143	234
$e^+e^- \rightarrow qq$	6,010,154	1,016
$\gamma_{\text{EPA}}e^- \rightarrow qqqqe^-$	430,643	20
$\gamma_{\text{BS}}e^- \rightarrow qqqqe^-$	1,741,050	42
$e^+\gamma_{\text{EPA}} \rightarrow qqqqe^+$	430,344	19
$e^+\gamma_{\text{BS}} \rightarrow qqqqe^+$	1,734,450	44
$\gamma_{\text{EPA}}e^- \rightarrow qqqq\nu$	48,893	3,552
$\gamma_{\text{BS}}e^- \rightarrow qqqq\nu$	205,326	18,540
$e^+\gamma_{\text{EPA}} \rightarrow qqqq\nu$	48,893	3,652
$e^+\gamma_{\text{BS}} \rightarrow qqqq\nu$	204,581	18,770
$\gamma_{\text{EPA}}\gamma_{\text{EPA}} \rightarrow qqqq$	1,129,459	68
$\gamma_{\text{EPA}}\gamma_{\text{BS}} \rightarrow qqqq$	6,052,200	55
$\gamma_{\text{BS}}\gamma_{\text{EPA}} \rightarrow qqqq$	6,027,979	0
$\gamma_{\text{BS}}\gamma_{\text{BS}} \rightarrow qqqq$	32,109,300	0

Table 2.9.: Number of events passing the MVA selection at 1.4TeV. Event numbers are normalised to the correct luminosity for CLIC at 1.4 TeV. The subscript EPA or BS for the incoming photons indicate whether the photon is generated from the equivalent photon approximation or beamstrahlung.

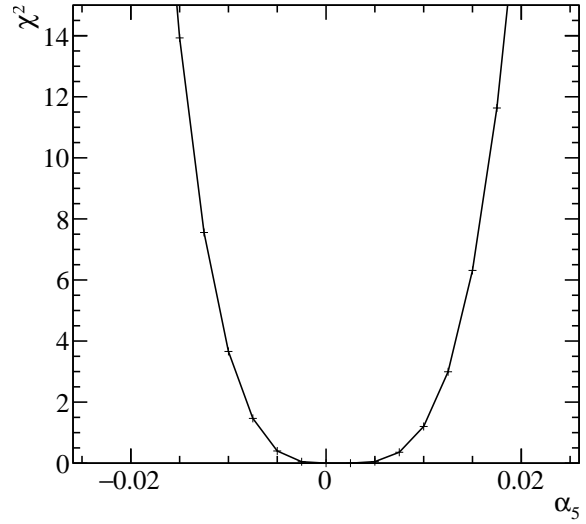
of preselection and MVA described in sections 2.7.1 and 2.7.2 purposed to remove the included background channels, described in section 2.2. These contours yield the one σ confidence limit on the measurement of α_4 to the range -0.00831, 0.0130 and similarly for the measurement of α_5 the range is -0.00606, 0.00904.



(a) χ^2 sensitivity contours in α_4 and α_5 space.



(b) χ^2 as a function of α_4 assuming $\alpha_5 = 0$.



(c) χ^2 as a function of α_5 assuming $\alpha_4 = 0$.

Figure 2.12.: χ^2 sensitivity distributions at 1.4 TeV arising from a fit to $\cos\theta_{\text{jets}}^*$. Results include the effect of backgrounds after the application of preselection and MVA.

Final State	ϵ_{presel}	ϵ_{BDT}	N_{BDT}
$e^+e^- \rightarrow \nu\nu qqqq$	56.7%	39.9%	14,770
$e^+e^- \rightarrow l\nu qqqq$	25.7%	3.7%	6,159
$e^+e^- \rightarrow \nu\nu qq$	4.3%	0.3%	3,286
$e^+e^- \rightarrow l\nu qq$	8.8%	0.1%	6,262
$\gamma_{\text{EPA}}e^- \rightarrow qqqq\nu$	18.0%	7.3%	3,552
$\gamma_{\text{BS}}e^- \rightarrow qqqq\nu$	23.2%	12.0%	18,540
$e^+\gamma_{\text{EPA}} \rightarrow qqqq\nu$	18.2%	7.5%	3,652
$e^+\gamma_{\text{BS}} \rightarrow qqqq\nu$	23.4%	12.2%	18,770

Table 2.10.: Selection summary at 1.4TeV. The subscript EPA or BS for the incoming photons indicate whether the photon is generated from the equivalent photon approximation or beamstrahlung.

Appendix A.

Pointless extras

*“Le savant n’étudie pas la nature parce que cela est utile;
il l’étudie parce qu’il y prend plaisir,
et il y prend plaisir parce qu’elle est belle.”*
— Henri Poincaré, 1854–1912

Appendixes (or should that be “appendices”?) make you look really clever, ‘cos it’s like you had more clever stuff to say than could be fitted into the main bit of your thesis. Yeah. So everyone should have at least three of them...

A.1. Anomalous Gauge Coupling Quartic Vertices Of Relevance in Vector Boson Scattering

The anomalous gauge couplings involving α_4 and α_5 arise in EFT through the addition of the following terms to the Lagrangian.

$$\text{Tr}(V^\mu V_\nu) \text{Tr}(V^\nu V_\mu) \text{ and } [\text{Tr}(V^\mu V_\mu)]^2 \quad (\text{A.1})$$

Where V_μ is defined in the following way.

$$V_\mu = \Sigma(D_\mu \Sigma)^\dagger \quad (\text{A.2})$$

and Σ , the Higgs field matrix, is defined as.

$$\Sigma = \exp\left(-\frac{i}{v}\mathbf{w}\right) \quad (\text{A.3})$$

Where $\mathbf{w} = w^a \sigma^a$. w^a are the ... and σ^a are the Pauli spin matrices. The covariant derivative of the Higgs field matrix is

$$D_\mu \Sigma = \left(\partial_\mu + \frac{ig}{2}W_\mu - \frac{ig'}{2}B_\mu\sigma^3\right)\Sigma \quad (\text{A.4})$$

For clarity consider the unitarity gauge where $\mathbf{w} = 0$, which implies $\Sigma = 1$. In this gauge V_μ takes the following form.

$$\begin{aligned} V_\mu &= \frac{i}{2}(gW_\mu^i\sigma^i - g'B_\mu\sigma^3) = \frac{i}{2} \begin{pmatrix} gW_\mu^3 - g'B_\mu & g(W_\mu^1 - iW_\mu^2) \\ g(W_\mu^1 + iW_\mu^2) & -gW_\mu^3 + g'B_\mu \end{pmatrix} \\ &= \frac{i}{2} \begin{pmatrix} \sqrt{g^2 + g'^2}Z_\mu & g\sqrt{2}W_\mu^+ \\ g\sqrt{2}W_\mu^- & \sqrt{g^2 + g'^2}Z_\mu \end{pmatrix} \end{aligned}$$

Where the relationship between the mass and gauge symmetry basis are as follows.

$$W_\mu^+ = \frac{1}{\sqrt{2}}(W_\mu^1 - iW_\mu^2) \quad (\text{A.5})$$

$$W_\mu^- = \frac{1}{\sqrt{2}}(W_\mu^1 + iW_\mu^2) \quad (\text{A.6})$$

$$Z_\mu = c_w W_\mu^3 - s_w B_\mu \quad (\text{A.7})$$

$$A_\mu = s_w W_\mu^3 + c_w B_\mu \quad (\text{A.8})$$

With $c_w = \frac{g}{\sqrt{g^2 + g'^2}}$ and $s_w = \frac{g'}{\sqrt{g^2 + g'^2}}$. Consider the expansion of the terms to be included in the Lagrangian.

$$V^\mu V_\nu = \frac{-1}{4} \begin{pmatrix} \sqrt{g^2 + g'^2} Z^\mu & g\sqrt{2} W^{+\mu} \\ g\sqrt{2} W^{-\mu} & \sqrt{g^2 + g'^2} Z^\mu \end{pmatrix} \begin{pmatrix} \sqrt{g^2 + g'^2} Z_\nu & g\sqrt{2} W_\nu^+ \\ g\sqrt{2} W_\nu^- & \sqrt{g^2 + g'^2} Z_\nu \end{pmatrix} \quad (\text{A.9})$$

$$\text{Tr}[V^\mu V_\nu] = \frac{-1}{2} ((g^2 + g'^2) Z^\mu Z_\nu + g^2 W^{+\mu} W_\nu^- + g^2 W^{-\mu} W_\nu^+) \quad (\text{A.10})$$

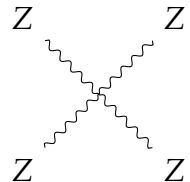
$$\text{Tr}[V^\mu V_\nu] \text{Tr}[V_\mu V^\nu] = \frac{(g^2 + g'^2)^2}{4} (Z^\mu Z_\mu)^2 + g^2 (g^2 + g'^2) (Z^\mu Z^\nu W_\mu^- W_\nu^+) \quad (\text{A.11})$$

$$+ \frac{g^4}{2} (W^{-\mu} W_\mu^+)^2 + \frac{g^4}{2} (W^{-\mu} W^{+\nu} W_\mu^- W_\nu^+) \quad (\text{A.12})$$

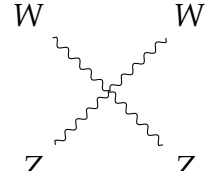
$$\text{Tr}[V^\mu V_\mu]^2 = \frac{(g^2 + g'^2)^2}{4} (Z^\mu Z_\mu)^2 + g^2 (g^2 + g'^2) (Z^\mu Z^\nu W_\mu^- W_\nu^+) \quad (\text{A.13})$$

$$+ g^4 (W^{-\mu} W_\mu^+)^2 \quad (\text{A.14})$$

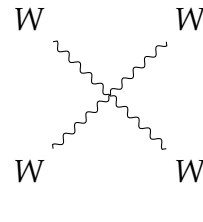
These two terms change the cross section for the vector boson scattering processes at CLIC that involve $ZZ \rightarrow ZZ$, $W^+ W^- \rightarrow ZZ$, $ZZ \rightarrow W^+ W^-$ and $W^+ W^- \rightarrow W^+ W^-$.



$$\subset (\alpha_4 + \alpha_5) \frac{(g^2 + g'^2)^2}{4} \quad (\text{A.15})$$



$$\subset (\alpha_4 + \alpha_5)g^2(g^2 + g'^2) \quad (\text{A.16})$$



$$\subset (\alpha_4 + 2\alpha_5)\frac{g^4}{2} \text{ and } \frac{g^4}{2}\alpha_4 \quad (\text{A.17})$$

A.2. χ^2 Contour Plots for Jet Algorithm Optimisation

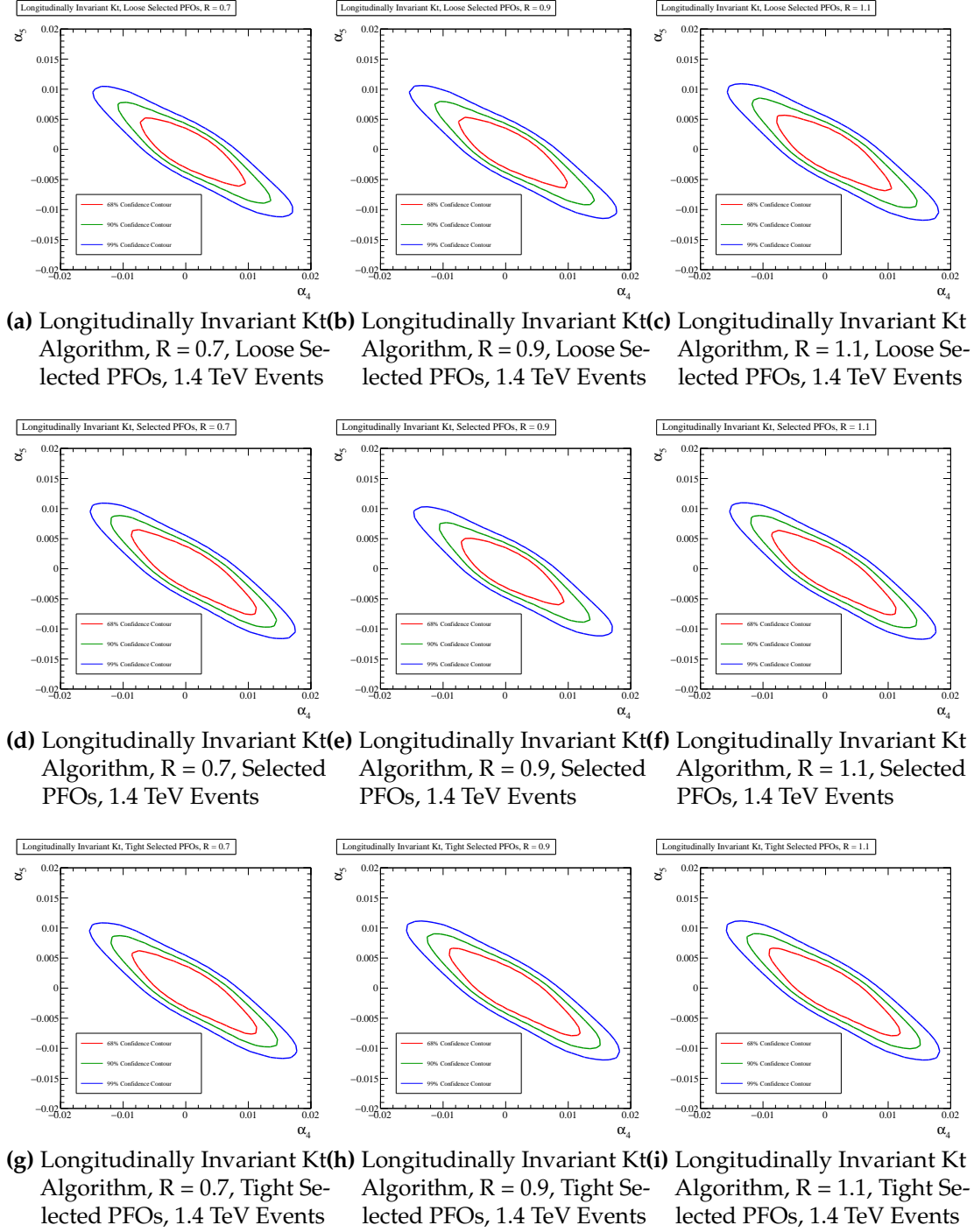


Figure A.1.: χ^2 Sensitivity contours for the $qqqq\nu\nu$ final state arising from a fit to $\cos\theta_{\text{jets}}^*$ at 1.4 TeV for different values of jet reconstruction parameters.

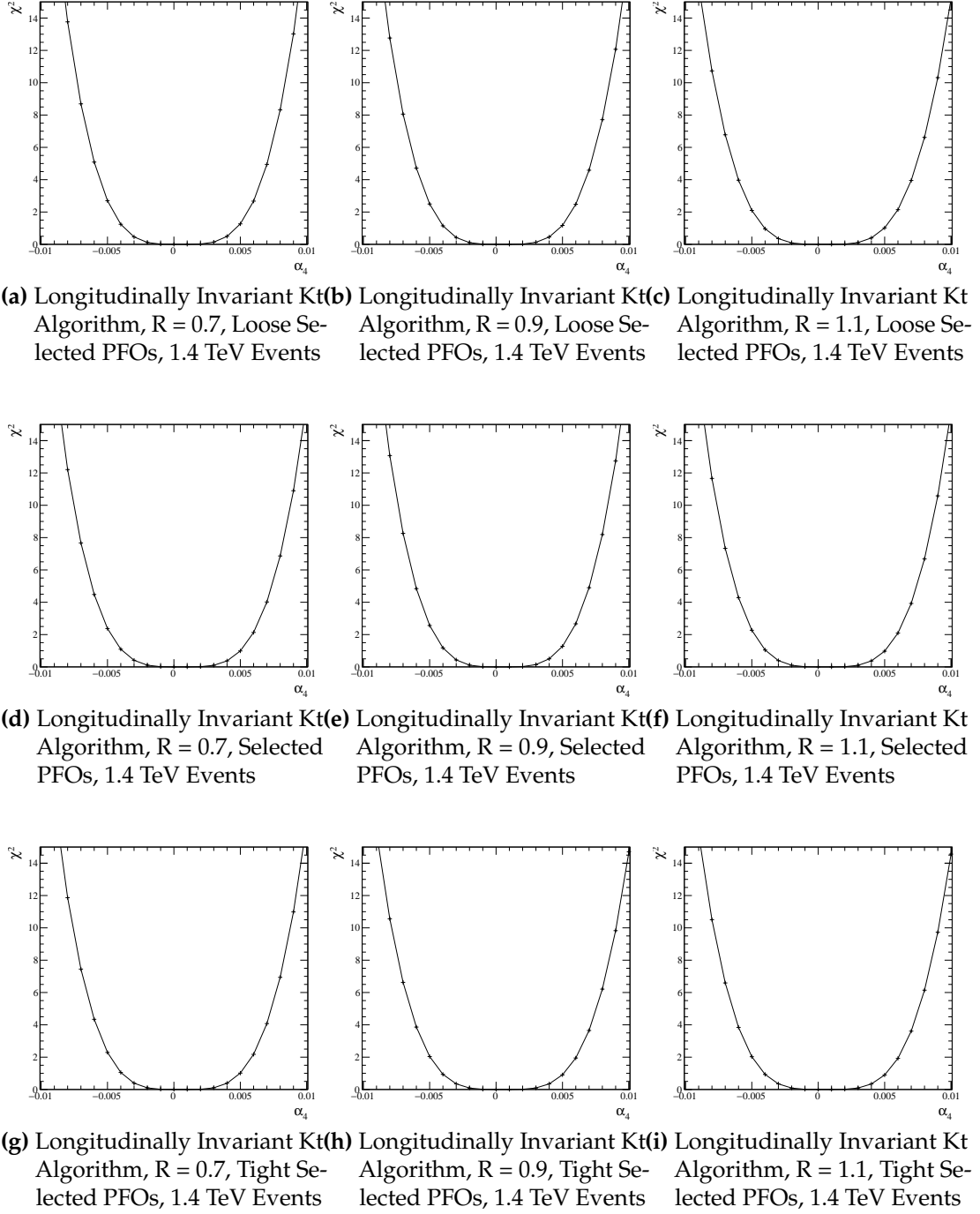


Figure A.2.: χ^2 as a function of α_4 assuming $\alpha_5 = 0$ for the $qqqq\nu\nu$ final state arising from a fit to $\cos\theta_{\text{jets}}^*$ at 1.4 TeV for different values of jet reconstruction parameters.

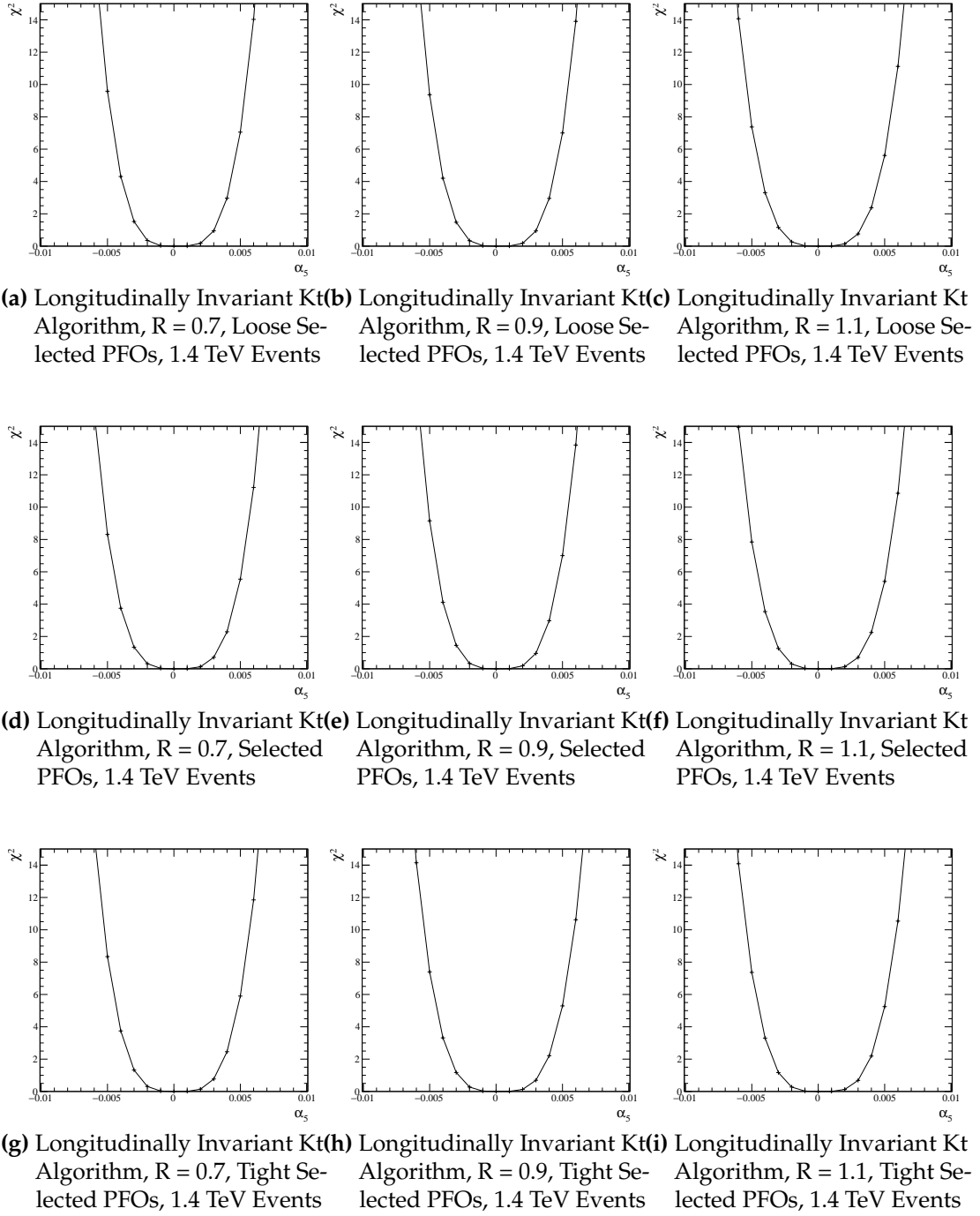
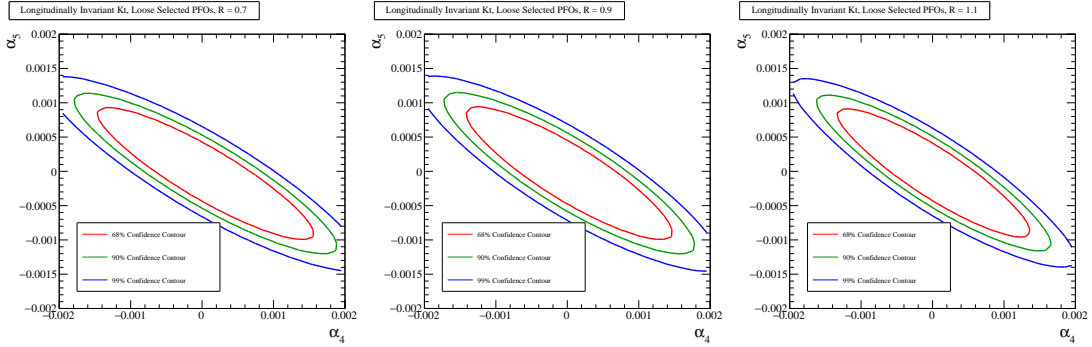


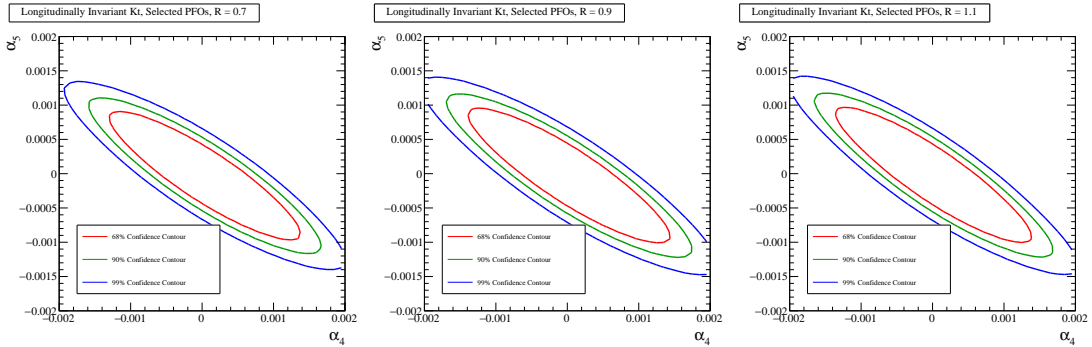
Figure A.3.: χ^2 as a function of α_5 assuming $\alpha_4 = 0$ for the $qqqq\nu\nu$ final state arising from a fit to $\cos\theta_{\text{jets}}^*$ at 1.4 TeV for different values of jet reconstruction parameters.



(a) Longitudinally Invariant Kt Algorithm, $R = 0.7$, Loose Selected PFOs, 3 TeV Events

(b) Longitudinally Invariant Kt Algorithm, $R = 0.9$, Loose Selected PFOs, 3 TeV Events

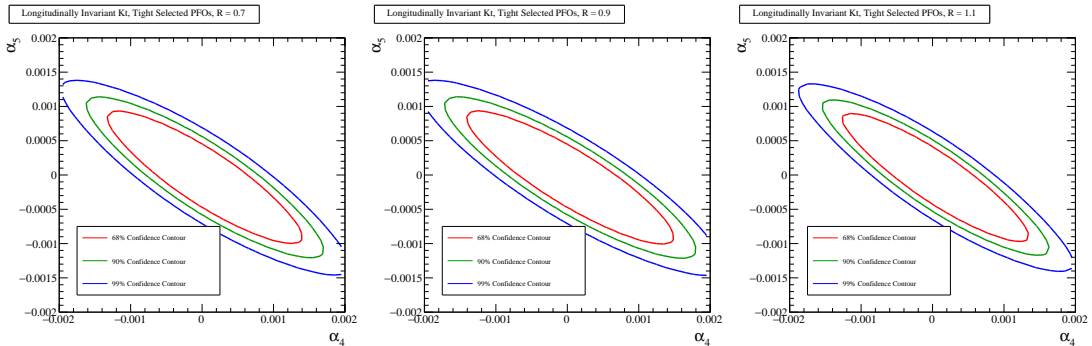
(c) Longitudinally Invariant Kt Algorithm, $R = 1.1$, Loose Selected PFOs, 3 TeV Events



(d) Longitudinally Invariant Kt Algorithm, $R = 0.7$, Selected PFOs, 3 TeV Events

(e) Longitudinally Invariant Kt Algorithm, $R = 0.9$, Selected PFOs, 3 TeV Events

(f) Longitudinally Invariant Kt Algorithm, $R = 1.1$, Selected PFOs, 3 TeV Events



(g) Longitudinally Invariant Kt Algorithm, $R = 0.7$, Tight Selected PFOs, 3 TeV Events

(h) Longitudinally Invariant Kt Algorithm, $R = 0.9$, Tight Selected PFOs, 3 TeV Events

(i) Longitudinally Invariant Kt Algorithm, $R = 1.1$, Tight Selected PFOs, 3 TeV Events

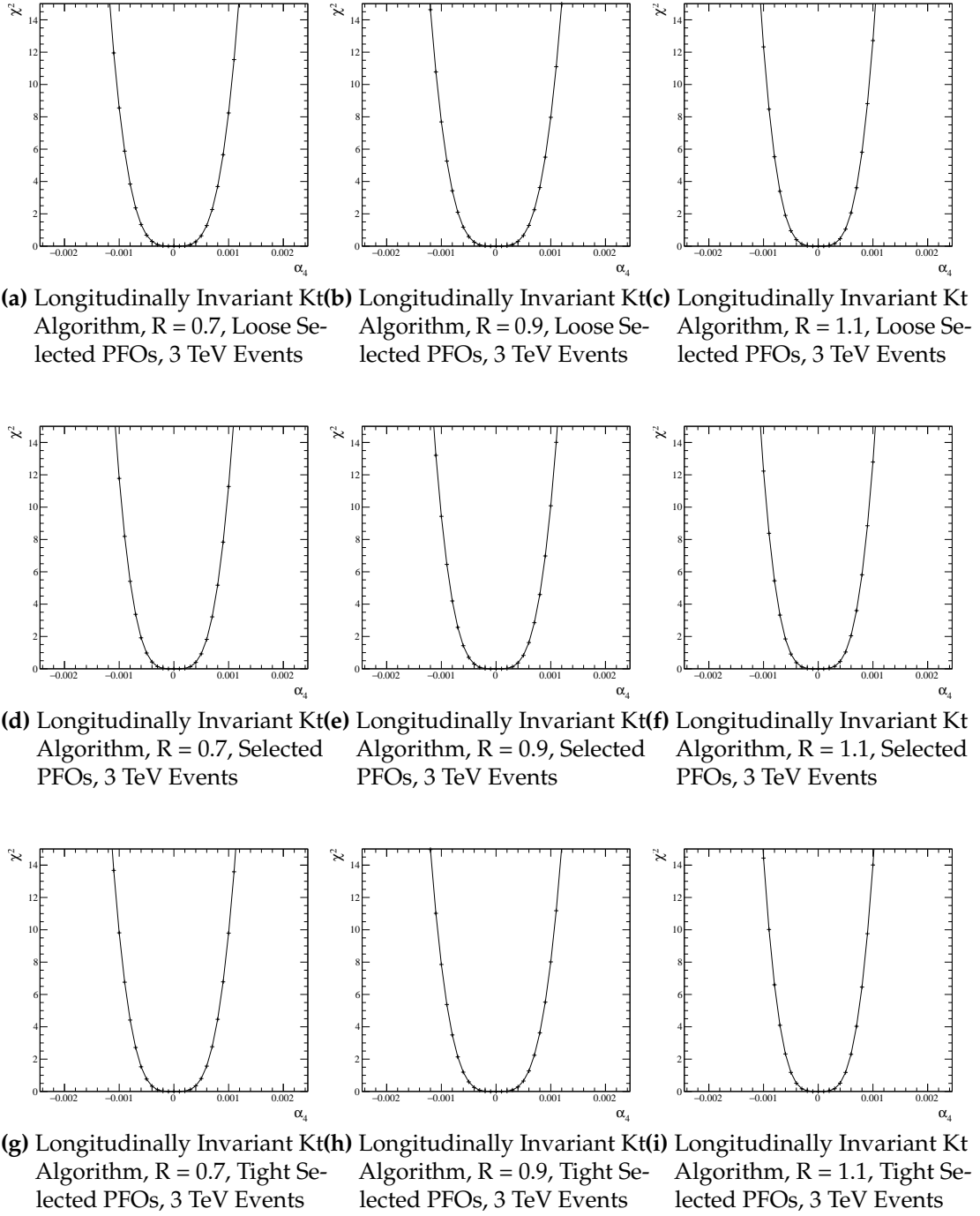


Figure A.4.: χ^2 as a function of α_4 assuming $\alpha_5 = 0$ for the $qqqq\nu\nu$ final state arising from a fit to $\cos\theta_{\text{jets}}^*$ at 3 TeV for different values of jet reconstruction parameters.

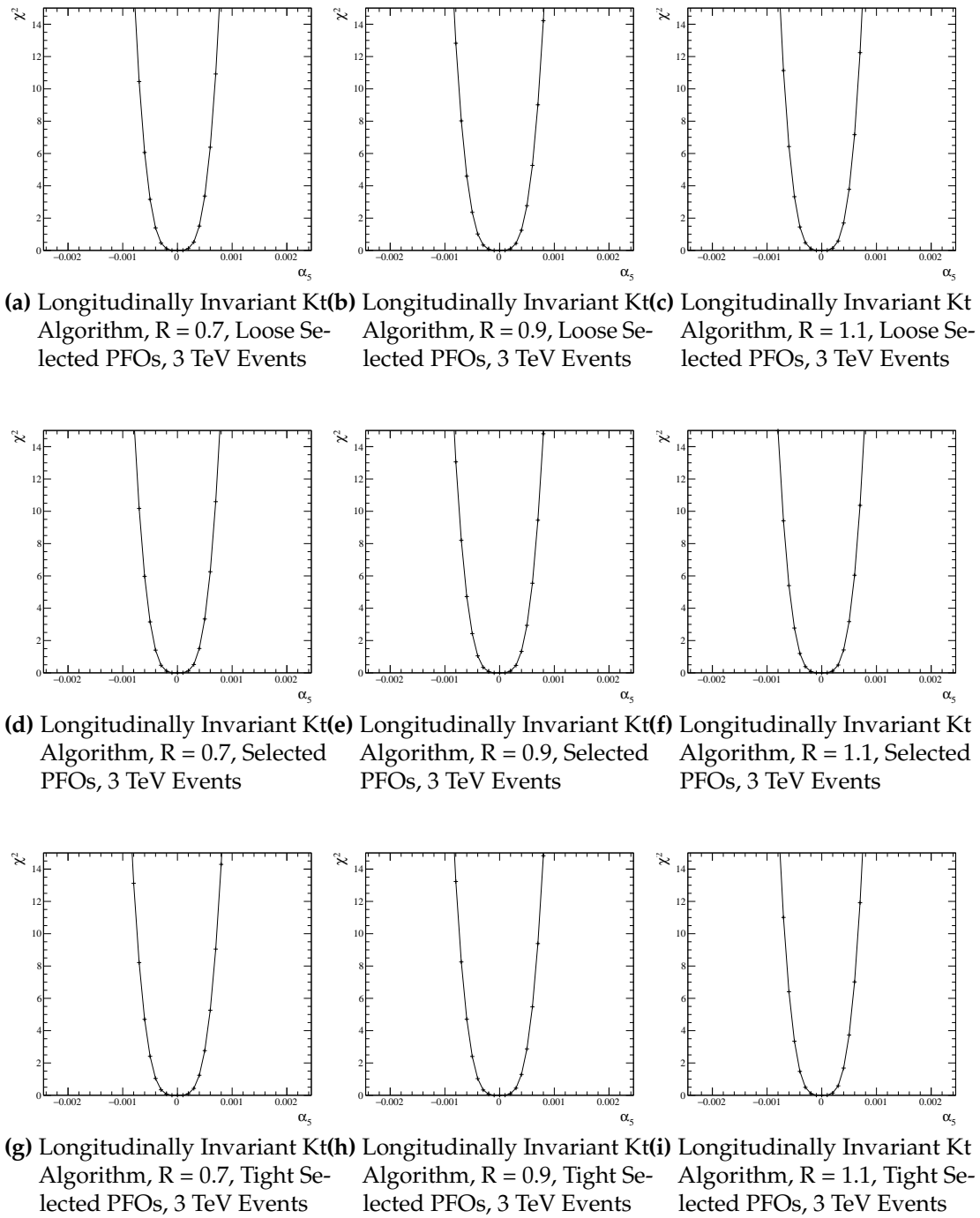


Figure A.5.: χ^2 as a function of α_5 assuming $\alpha_4 = 0$ for the $qqqq\nu\nu$ final state arising from a fit to $\cos\theta_{\text{jets}}^*$ at 3 TeV for different values of jet reconstruction parameters.

Colophon

This thesis was made in $\text{\LaTeX}2_{\epsilon}$ using the “hepthesis” class [3].

Bibliography

- [1] Toshinori Abe et al. The International Large Detector: Letter of Intent. 2010, 1006.3396.
- [2] S. Agostinelli et al. GEANT4: A Simulation toolkit. *Nucl. Instrum. Meth.*, A506:250–303, 2003.
- [3] Andy Buckley. The hepthesis L^AT_EX class.
- [4] Matteo Cacciari, Gavin P. Salam, and Gregory Soyez. FastJet User Manual. *Eur. Phys. J.*, C72:1896, 2012, 1111.6097.
- [5] F. Gaede. Marlin and LCCD: Software tools for the ILC. *Nucl. Instrum. Meth.*, A559:177–180, 2006.
- [6] Andreas Hoecker, Peter Speckmayer, Joerg Stelzer, Jan Therhaag, Eckhard von Toerne, and Helge Voss. TMVA: Toolkit for Multivariate Data Analysis. *PoS, ACAT:040*, 2007, physics/0703039.
- [7] Wolfgang Kilian, Thorsten Ohl, and Jurgen Reuter. WHIZARD: Simulating Multi-Particle Processes at LHC and ILC. *Eur. Phys. J.*, C71:1742, 2011, 0708.4233.
- [8] Lucie Linssen, Akiya Miyamoto, Marcel Stanitzki, and Harry Weerts. Physics and Detectors at CLIC: CLIC Conceptual Design Report. 2012, 1202.5940.
- [9] J. S. Marshall, A. Mäijnnich, and M. A. Thomson. Performance of Particle Flow Calorimetry at CLIC. *Nucl. Instrum. Meth.*, A700:153–162, 2013, 1209.4039.
- [10] P. Mora de Freitas and H. Videau. Detector simulation with MOKKA / GEANT4: Present and future. In *Linear colliders. Proceedings, International Workshop on physics and experiments with future electron-positron linear colliders, LCWS 2002, Seogwipo, Jeju Island, Korea, August 26-30, 2002*, pages 623–627, 2002.
- [11] Mauro Moretti, Thorsten Ohl, and Jurgen Reuter. O’Mega: An Optimizing matrix

- element generator. 2001, hep-ph/0102195.
- [12] C. Patrignani et al. Review of Particle Physics. *Chin. Phys.*, C40(10):100001, 2016.
- [13] Andr   Sailer. *Radiation and Background Levels in a CLIC Detector due to Beam-Beam Effects*. PhD thesis, CERN, 2012-05-09.
- [14] Taikan Suehara and Tomohiko Tanabe. LCFIPlus: A Framework for Jet Analysis in Linear Collider Studies. *Nucl. Instrum. Meth.*, A808:109–116, 2016, 1506.08371.
- [15] M. A. Thomson. Particle Flow Calorimetry and the PandoraPFA Algorithm. *Nucl. Instrum. Meth.*, A611:25–40, 2009, 0907.3577.

List of figures

1.1. Energy resolution as a function of photon energy for the nominal ILD detector for both the silicon and scintillator options.	2
1.2. Jet energy resolution as a function of ECal cell size.	4
1.3. Jet energy resolution breakdown as a function of ECal transverse granularity for 45 and 250 GeV jets. Results are given for both the silicon and scintillator ECal options.	5
1.4. Energy resolution as a function of ECal transverse granularity for 100 GeV photons. Results are given for both the silicon and scintillator ECal options.	5
1.5. Jet energy resolution as a function of longitudinal granularity in the ECal.	7
1.6. Jet energy resolution breakdown as a function of ECal longitudinal granularity for 45 and 250 GeV jets. Results are given for both the silicon and scintillator ECal options.	8
1.7. Energy resolution as a function of ECal longitudinal granularity for 100 GeV photons. Results are given for both the silicon and scintillator ECal options.	8
1.8. Jet energy resolution as a function of HCal cell size.	11
1.9. Jet energy resolution breakdown as a function of HCal transverse granularity for 45 and 250 GeV jets.	12
1.10. Energy resolution as a function of HCal transverse granularity for 50 GeV K_L^0	12
1.11. Jet energy resolution as a function of longitudinal granularity in the HCal.	13

1.12. Jet energy resolution breakdown as a function of HCal longitudinal granularity for 45 and 250 GeV jets.	14
1.13. Energy resolution as a function of HCal longitudinal granularity for 50 GeV K_L^0	15
1.14. Jet energy resolution as a function of the number of nuclear interaction lengths in the HCal.	16
1.15. Jet energy resolution breakdown as a function of nuclear interaction lengths in the HCal for 45 and 250 GeV jets.	17
2.1. Event weights from Whizard for 1.4TeV $\nu\nu qqqq$ final state events. . . .	23
2.2. Comparison of various distributions between samples used in this analysis and the official CLIC samples for the $\nu\nu qqqq$ final state and 1.4 TeV.	24
2.4. Reconstructed invariant masses for different choices of jet algorithm for 1.4 TeV and 3 TeV $\nu\nu qqqq$ events.	29
2.5. Sensitivity of $\cos\theta_{jets}^8$ to the anomalous gauge couplings α_4 and α_5 at 1.4 and 3 TeV.	33
2.6. Sensitivity of $\cos\theta_{Bosons}^8$ to the anomalous gauge couplings α_4 and α_5 at 1.4 and 3 TeV.	34
2.7. Event weights from Whizard for 1.4TeV $\nu\nu qqqq$ final state events with interpolated surface.	35
2.8. χ^2 sensitivity distributions for the $qqqq\nu\nu$ final state arising from a fit to $\cos\theta_{jets}^*$ at 1.4 TeV for the optimal jet reconstruction parameters. . . .	38
2.9. χ^2 sensitivity distributions for the $qqqq\nu\nu$ final state arising from a fit to $\cos\theta_{jets}^*$ at 3 TeV for the optimal jet reconstruction parameters. . . .	40
2.10. Distribution of variables cut on in the preselection at 1.4 TeV.	43
2.11. Impact of preselection and MVA on the reconstructed invariant mass of the bosons arising from jet pairing at 1.4 TeV.	46

2.12. χ^2 sensitivity distributions at 1.4 TeV arising from a fit to $\cos\theta_{\text{jets}}^*$. Results include the effect of backgrounds after the application of preselection and MVA.	48
A.1. χ^2 Sensitivity contours for the $qqqq\nu\nu$ final state arising from a fit to $\cos\theta_{\text{jets}}^*$ at 1.4 TeV for different values of jet reconstruction parameters.	55
A.2. χ^2 as a function of α_4 assuming $\alpha_5 = 0$ for the $qqqq\nu\nu$ final state arising from a fit to $\cos\theta_{\text{jets}}^*$ at 1.4 TeV for different values of jet reconstruction parameters.	56
A.3. χ^2 as a function of α_5 assuming $\alpha_4 = 0$ for the $qqqq\nu\nu$ final state arising from a fit to $\cos\theta_{\text{jets}}^*$ at 1.4 TeV for different values of jet reconstruction parameters.	57
A.4. χ^2 as a function of α_4 assuming $\alpha_5 = 0$ for the $qqqq\nu\nu$ final state arising from a fit to $\cos\theta_{\text{jets}}^*$ at 3 TeV for different values of jet reconstruction parameters.	59
A.5. χ^2 as a function of α_5 assuming $\alpha_4 = 0$ for the $qqqq\nu\nu$ final state arising from a fit to $\cos\theta_{\text{jets}}^*$ at 3 TeV for different values of jet reconstruction parameters.	60

List of tables

1.1. Nominal ILD detector model ECal configuration.	3
1.2. Transverse granularity layout of various ECal models considered in this study.	7
1.3. Nominal ILD detector model HCal configuration.	10
1.4. Transverse granularity layout of various HCal models considered. . . .	14
1.5. Depth and layout of various HCal models considered.	16
2.1. Cross section for selected processes for given value of α_4 and α_5 at 1.4 TeV.	22
2.2. Cross section for selected processes for given value of α_4 and α_5 at 3 TeV.	22
2.3. 1σ precision on measurement of α_4 for different jet reconstruction parameters considering pure signal at 1.4 TeV.	37
2.4. 1σ precision on measurement of α_5 for different jet reconstruction parameters considering pure signal at 1.4 TeV.	37
2.5. 1σ precision on measurement of α_4 for different jet reconstruction parameters considering pure signal at 3 TeV.	39
2.6. 1σ precision on measurement of α_5 for different jet reconstruction parameters considering pure signal at 3 TeV.	39
2.8. Number of events passing the various cuts applied in the preselection at 1.4TeV.	44
2.9. Number of events passing the MVA selection at 1.4TeV.	47
2.10. Selection summary at 1.4TeV.	49